Aus dem Institut für Computerunterstützte Klinische Medizin
der Medizinischen Fakultät Mannheim
(Direktor: Prof. Dr. rer. nat. Lothar R. Schad)

Differentiation of glioblastoma and cerebral metastasis using MR-derived tissue oxygenation and perfusion: a machine learning approach

Inauguraldissertation
zur Erlangung des medizinischen Doktorgrades
der
Medizinischen Fakultät Mannheim
der Ruprecht-Karls-Universität
zu
Heidelberg

vorgelegt von
Hakim Baazaoui

aus
Bad Soden am Taunus
2021

Dekan: Prof. Dr. med. Sergij Goerdt
Referent: Prof. Dr. rer. nat. Lothar Schad

To my parents

TABLE OF CONTENTS

LIST OF FIGURES

LIST OF TABLES

ABBREVIATIONS

2D	two-dimensional
3D	three-dimensional
ANN	artificial neural network
ASL	arterial spin labeling / arterial spin-labeled
AUC	area under the curve
BIC	Bayesian information criterion
BOLD	blood-oxygenation-level-dependent
CBF	cerebral blood flow
CBV	cerebral blood volume
CET	contrast-enhancing tumor
cMET	cerebral metastasis
$CMRO_2$	cerebral metabolic rate of oxygen
cNAB	contralateral normal-appearing brain
CSF	cerebrospinal fluid
FLAIR	fluid attenuated inversion recovery
fMRI	functional magnetic resonance imaging
GBM	glioblastoma
IDH	isocitrate dehydrogenase
ISMRM	International Society for Magnetic Resonance in Medicine
KNN	k-nearest neighbor
MGMT	O-6-methylguanine-DNA-methyltransferase
mGRE	multi-gradient echo
MPRAGE	magnetization-prepared rapid gradient echo
MRI	magnetic resonance imaging
nCBF	normalized cerebral blood flow
NET2	non-enhancing T2 FLAIR hyperintense region

ABBREVIATIONS

OEF	oxygen extraction fraction
pCASL	pseudo-continuous arterial spin labeling
PET	positron emission tomography
PFS	progression-free survival
PLD	post-labeling delay
qBOLD	quantitative blood-oxygenation-level-dependent
QSM	quantitative susceptibility mapping
rCBF	relative cerebral blood flow
rCBV	relative cerebral blood volume
ROC	receiver operating characteristic
rOEF	relative oxygen extraction fraction
rOER	regional oxygen extraction ratio
ROI	region of interest
SNR	signal-to-noise ratio
SVM	support-vector machine
VEGF	vascular endothelial growth factor
vWF	von Willebrand factor
WHO	World Health Organization

1 INTRODUCTION

1.1 Background and current diagnostic difficulties

Glioblastoma and cerebral metastasis are the most common brain tumors in adult patients (Lee et al., 2011). Glioblastoma is a high-grade glioma that can emerge either as a primary or secondary brain tumor from lower-grade astrocytoma, for instance after initial therapy (Noroxe et al., 2016). It constitutes between 60% and 70% of all malignant gliomas (Wen and Kesari, 2008). The World Health Organization (WHO) classifies glioblastoma as a high-grade glioma with the highest possible WHO grade IV, as necrosis-prone, wildly infiltrative with rapid and aggressive growth and fast recurrence (AANS, 2021). Median survival for this highly malignant entity is estimated to be 12 – 15 months with optimal treatment (Wen and Kesari, 2008), which consists of a combination of surgical resection, radiation and chemotherapy (Stupp et al., 2005).

With regards to brain metastases, over 20% of cancer patients develop disseminations to the central nervous system, mostly through hematogenous spread (AANS, 2021), thus making them the most commonly diagnosed type of cerebral tumor (Ostrom et al., 2018). The tumors that are most likely to metastasize to the brain are lung cancer, renal cell carcinoma and breast cancer as well as melanoma (Tabouret et al., 2012). The incidence of these tumors is increasing as advanced imaging techniques lead to earlier diagnoses and as new systemic treatments and better screening become available, making longer survival after initial diagnosis of the primary cancer possible and therefore leaving more time for tumors to metastasize (Nayak et al., 2012). Metastatic lesions typically grow at the border of white and gray matter (Gavrilovic and Posner, 2005). In the case of a solitary brain metastasis it has been shown that the best available treatment in terms of survival and quality of life consists of aggressive surgical management in combination with radiation therapy, but when multiple brain metastases are present, the benefit for patients of aggressive surgical resection and radiation is less obvious (AANS, 2021). In the presence of multiple metastases, multidisciplinary therapy decisions should be made dependent on the particularities of the patient, i.e. general condition, acutely life-threatening tumor growth and the extent of cancer elsewhere in the body (Suh et al., 2020).

Due to its pronounced soft tissue contrast, magnetic resonance imaging (MRI), both non-contrast and enhanced with gadolinium-based agents, is the radiological tool of choice for diagnosis of intracerebral tumors. It might prove difficult, however, to reliably differentiate a metastasis from a glioblastoma without known history of a primary tumor due to their similar radiological appearance in MRI (Li et al., 2020; Bauer et al., 2015). One study identified 55% of brain metastasis cases to have had no known primary at diagnosis (Giordana et al., 2000). In addition, between 30% and 50% of brain metastases appear solitary at diagnosis, further complicating a reliable differential diagnosis (Bauer et al., 2015; Server et al., 2011; Blasel et al., 2010). To make matters even more difficult, both tumor types can show necrotic centers, contrast-enhancing peripheral areas signaling a disruption disrupted blood-brain barrier and extensive peritumoral edema (Artzi et al., 2019).

Moreover, when relying solely on contrast-enhanced imaging, it is virtually impossible to detect infiltration before disruption of the blood-brain barrier (Young, 2007). In T2-weighted images, peritumoral hyperintensities can be present in both entities, further complicating their visual distinction. The hyperintense region around the enhancing part of glioblastomas is visible because of an increased vascular permeability of newly-sprouted vessels whose growth has been induced by hypoxic tumor tissue, leading to vasogenic edema (Lehmann et al., 2012). The peritumoral T2 hyperintense regions are known to also contain tumor cell infiltrates

in glioblastomas while they are caused by purely vasogenic edema in brain metastases (Fink and Fink, 2013). This dilemma is illustrated by the comparison of a cerebral metastasis and a glioblastoma in Figure 1, with both tumors displaying cystic necrosis and peripheral contrast enhancement. Accurately discriminating between the two is of great clinical importance because tumor staging, treatment approach, and surgical decisions are quite different and directly affect clinical outcomes (Server et al., 2011). The current diagnostic gold standard is an invasive tissue biopsy with subsequent histopathological examination (Lee et al., 2013), a procedure that, with a complication rate of about 6%, is not without inherent risk (Malone et al., 2015).

(a)   **(b)**
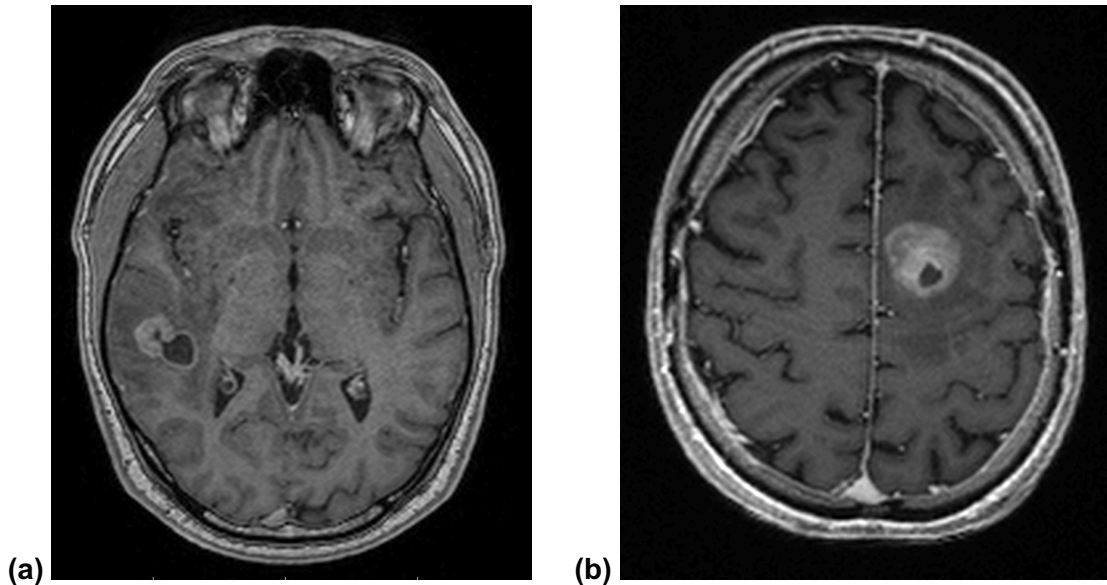
Figure 1:   Axial T1-weighted contrast-enhanced brain images comparing **(a)** a right temporal metastasis from known esophageal cancer in a 50-year-old male patient and **(b)** a glioblastoma in the frontal lobe of the left hemisphere of a 71-year-old male patient. Both tumors show cystic elements and peripheral contrast enhancement, complicating a differentiation based on solely morphological criteria.

The metabolism of glioblastoma cells is adapted to the increased uptake of nutrients (mainly nucleotides, amino acids and lipids) into the tumor (Stadlbauer et al., 2020). To make that possible, cancer cells utilize aerobic glycolysis, a mechanism originally proposed in the 1920s (Warburg et al., 1927) and subsequently coined as *Warburg effect*. Although benefiting from increased perfusion and greater supply of components for cell upkeep, glioblastomas frequently grow too fast for their vasculature, eventually reaching a point at which central parts of the tumor cannot be maintained anymore (Wen and Kesari, 2008), resulting in the typical central necrosis and peripheral hyperintensity in T1-weighted, contrast-enhanced MR images (Noroxe et al., 2016).

Likewise, a similar pattern can be observed in the neuroimaging of brain metastases stemming from different primary cancers (Smirniotopoulos et al., 2007). Cerebral metastases are often found as smaller, solidly enhancing lesions in earlier stages before developing a necrotic center due to them outgrowing their blood and nutrient supply, hence becoming ring-enhancing (Pope, 2018).

INTRODUCTION

1.2   Literature review on the differentiation of glioblastoma and cerebral metastasis

The discrimination of glioblastoma and cerebral metastasis with radiological means has been tried many a time using a variety of different approaches, some more successful than others, due to the inherent challenges stemming from overlapping imaging features (Shrot et al., 2019). A lot of recent studies have focused on using dynamic susceptibility contrast sequences to evaluate perfusion metrics, most commonly cerebral blood volume (CBV) (Li et al., 2020; Swinburne et al., 2019; Askaner et al., 2019; Server et al., 2011). Another method that has been tested previously is pseudo-continuous arterial spin labeling (pCASL) based perfusion estimation. It yields cerebral blood flow (CBF) which has been used for comparison of perfusion in enhancing tumor regions and in peritumoral T2-weighted hyperintensities (Abdel Razek et al., 2019; Sunwoo et al., 2016). CBF in peritumoral tissue has also been used to determine perfusion gradients around the lesions in question in order to achieve greater diagnostic accuracy (Lin et al., 2016).

The majority of studies found no significant perfusion differences in regions of interest (ROIs) within the solid-appearing contrast-enhancing tumor and the areas outside of the peritumoral hyperintensity, present in T2-weighted imaging, between patients suffering from glioblastoma and from cerebral metastasis. Relative cerebral blood volume (rCBV = CBV in region of interest divided by CBV in normal-appearing white matter) in the proximal peritumoral T2 hyperintensity was found to be significantly higher in glioblastomas than in metastases (Askaner et al., 2019; Tsolaki et al., 2013; Lehmann et al., 2012). In the distal parts of the peritumoral T2 fluid attenuated inversion recovery (FLAIR) hyperintensity, glioblastoma and metastasis showed similar rCBV values which may reflect a lack of glioblastoma cell infiltration and angiogenesis, supporting the notion that angiogenesis follows a gradient around the tumor (Lehmann et al., 2012).

With regards to oxygenation, tissue hypoxia has been associated with higher tumor grade and the use of hypoxia as a predictor of therapy resistance to radiation therapy and/or chemotherapy is widely accepted (Preibisch et al., 2017). However, identifying hypoxic tissue has presented itself as a considerable obstacle in MRI (ibid.). As it can give information about physiological and pathological oxygenation processes in the brain, oxygen extraction fraction (OEF) is highly relevant in clinical research: prominent examples of studies investigating relative and absolute (r)OEF in gliomas based on the blood-oxygenation-level-dependent (BOLD) effect looked at the application of this metric as part of multiparametric models in conjunction with contrast-enhanced MR images and perfusion metrics. In one instance, it was used for differentiation of WHO grade II/III glioma from WHO grade IV glioblastoma (Wiestler et al., 2016). Another application of BOLD-derived OEF was the characterization of isocitrate dehydrogenase (IDH) mutation status in gliomas where the cerebral metabolic rate of oxygen ($CMRO_2$) emerged as the feature with the highest diagnostic performance for detection of IDH gene mutation in these malignant brain tumors (Stadlbauer et al., 2017b). MR-derived OEF and $CMRO_2$ were also very recently used as parts of an examination of the tumor microenvironment and metabolic phenotype switching, from a glycolytic phenotype with a stable vasculature to a necrotic/hypoxic phenotype with largely defective neovasculature and vice versa, in patients with recurrent glioblastoma (Stadlbauer et al., 2020). Based on these results, it was hypothesized that hypoxia triggers the switch from a proliferative to an invasive phenotype as part of a "survival strategy" of glioblastoma cells to evade a hypoxic tumor microenvironment. Hypoxia, however, also stimulates the growth of new blood vessels via the induction and release of vascular endothelial growth factor (VEGF), thereby enabling proliferating glioblastoma cells to sustain the energy demands of continued tumor growth (Stadlbauer et al., 2020).

INTRODUCTION

Several mechanisms of how high-grade gliomas induce the growth of their own vessels have been discovered: Vascular co-option, present in both low-grade gliomas and the infiltrative growth zone of high-grade gliomas, is followed by the development of new vessels via four more kinds of neovascularization. These consist of angiogenesis, vasculogenesis, vascular mimicry, and transdifferentiation of glioma cells into endothelial cells (Hardee and Zagzag, 2012). This neovascularization leads to a dilated and tortuous vessel configuration, abnormal branching and arteriovenous shunts (ibid.). These inefficiencies in the vasculature are correlated with greatly increased tumor perfusion, lower OEF and, in sum, a higher $CMRO_2$ (Stadlbauer et al., 2017b). Earlier investigations, frequently based on the BOLD effect, showed generally low intratumoral OEF values in patients suffering from glioma, confirming the results of previous ^{15}O positron emission tomography (PET) studies which are widely regarded as the reference standard for OEF and $CMRO_2$ measurements (Preibisch et al., 2017; Fan et al., 2020). But since ^{15}O has a very short half-life of just over two minutes, this image acquisition method requires a cyclotron on-site, making it technically difficult and expensive (Hubertus, 2019).

1.3   Research gap and objective of the study

In this study, MR-derived oxygen extraction fraction, cerebral blood flow and cerebral metabolic rate of oxygen were calculated and compared in patients with glioblastoma and cerebral metastasis. OEF was estimated using a combination of quantitative susceptibility mapping and the quantitative blood-oxygenation-level-dependent effect (QSM + qBOLD) which was introduced in 2018 (Cho et al., 2018). Parameter maps calculated with the QSM + qBOLD model have shown higher, more uniform OEF across the whole brain than QSM or qBOLD alone, confirming the findings of previous PET studies (Cho et al., 2018). Two different machine learning-based approaches for performing the QSM + qBOLD analysis on 3D multi-gradient echo (mGRE) data were employed and compared: an artificial neural network (ANN) (Hubertus et al., 2019a) and an X-means clustering approach (Cho et al., 2020).

The qBOLD approach was initially proposed in 1994 (Yablonskiy and Haacke, 1994) and subsequently adapted for modelling of OEF by inferring the oxygenation of brain tissue from the magnitude of the MRI signal (He and Yablonskiy, 2007). In turn, the postprocessing method QSM was introduced in 2010 (de Rochefort et al., 2010), allowing for reconstruction of the magnetic susceptibility of tissue using the phase of the MRI signal.

In this study, CBF was calculated with a pCASL sequence that uses blood as endogenous contrast agent for perfusion estimation. OEF and CBF together allow for the computation of $CMRO_2$, which can serve as a marker of intratumoral angiogenesis and oxygenation status (Kickingereder et al., 2020). With the QSM + qBOLD technique combining both magnitude and phase of the MR signal, $CMRO_2$ estimates have been demonstrated to be more robust, better reproducing results from earlier PET studies when compared to QSM or qBOLD alone (Cho et al., 2018).

The concept of combining oxygen extraction fraction with cerebral blood flow, thereby arriving at the cerebral metabolic rate of oxygen, is new for differentiating glioblastoma from cerebral metastasis. To the best of the author's knowledge, no prior research has applied these methods to said tumor entities, making this the first study to systematically compare and differentiate glioblastoma and cerebral metastasis using the combined QSM + qBOLD approach. It was the aim of this study to apply this method for the first time to a prospectively recruited collective of glioblastoma and brain metastasis patients and compare their cerebral oxygenation and perfusion. Based on the hypothesis that the infiltrative growth of glioblastomas and

the lack thereof in cerebral metastases (Sunwoo et al., 2016) would create discernable OEF and CBF patterns, a number of machine learning classifiers was trained to reliably differentiate the two entities, analyzing the oxygenation and perfusion parameters in and around the contrast-enhancing tumor.

2 MATERIALS AND METHODS

2.1 Patients

Between December 2019 and October 2020, 15 patients with primary glioblastoma (n = 7; median age: 68 years, range: 54–84 years) or cerebral metastasis from extracerebral primary tumors (n = 8; median age: 66 years, range: 50–78 years) before resection, radiation or chemotherapy were prospectively included in this study. Ten patients were male, five were female. A further two patients were excluded from the study due to their respective histopathological diagnoses of low-grade glioma and cerebral Hodgkin's lymphoma. Diagnoses were confirmed through histopathological examination. Metastatic lesions originated from four lung tumors, one esophageal carcinoma and three cancers of unknown primary. The study was approved by the ethics commission of the Mannheim Medical Faculty (reference: 2017-666N-MA). Written informed consent was obtained from every participant prior to MRI measurements and the acquired MRI image data was anonymized before further processing.

2.2 Image acquisition

2.2.1 Scanner

All MRI scans were performed on a 3T MAGNETOM Trio system (Siemens Healthcare GmbH, Erlangen, Germany) at the Department of Neuroradiology of the Mannheim Medical Faculty. The data of the first two patients were acquired using a 32-channel head coil. Due to practical reasons in clinical day-to-day MRI scans, all subsequent study participants were measured with a 12-channel head coil that is used for signal detection in most other neuroradiological sequences on the Trio scanner.

2.2.2 Sequences

The MRI protocol included a 3D multi-gradient echo (mGRE), an unbalanced axial two-dimensional pseudo-continuous arterial spin labeling (2D pCASL; 3D pCASL was employed for the first two patients that were scanned with a 32-channel head coil) and a T1-weighted magnetization prepared rapid gradient echo (T1 MPRAGE) sequence. The gadolinium-based contrast agent Dotarem® (Guerbet SA, Villepinte, France) was administered as bolus injection for the T1-weighted sequence at a dosage of 0.1ml per kg body weight. The labeling plane for the pCASL sequence was placed circa 85mm inferior to the anterior commissure-posterior commissure line, approximately perpendicular to the feeding arteries, in line with the consensus recommendations for arterial spin-labeled (ASL) imaging (Alsop et al., 2015). The sequences and specific parameters used in this study have all been published and described in detail (Hubertus, 2019).

MATERIALS AND METHODS

2.3 Image processing

The images obtained from the aforementioned MRI sequences were registered using the statistical parametric mapping software SPM12 (The Wellcome Centre for Human Neuroimaging, UCL Queen Square Institute of Neurology, London, UK) using default values. Post-processing was performed with MATLAB R2020b (MathWorks, Natick, MA, USA) (Hubertus, 2019). In order to calculate perfusion and oxygenation parameters for specific regions in the brain, three regions of interest were drawn manually. To obtain masks for contrast-enhancing tumor (CET) ROIs were drawn manually around the entire contrast-enhancing tumor in T1-weighted images on all slices where it was present and automatically mirrored at the midline of the brain to generate a cNAB ROI (cf. Figure 2).
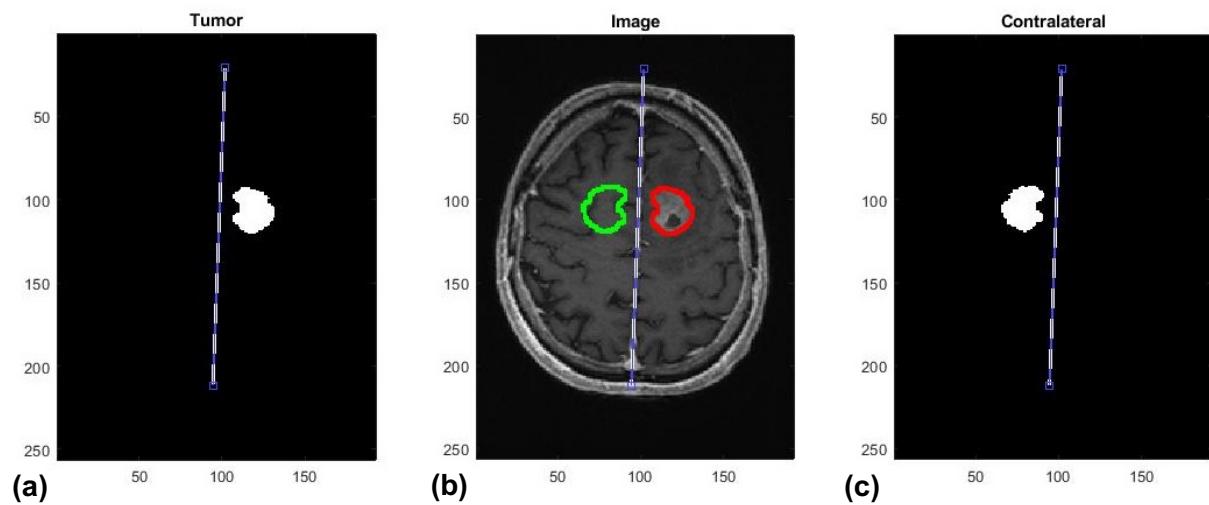
Figure 2: Axial T1-weighted contrast-enhanced image of a 71-year-old male glioblastoma patient. Panel **(a)** shows an image of the contrast-enhancing tumor ROI, extracted from panel **(b)**, which displays two ROIs: the red ROI is drawn around the contrast-enhancing tumor and then mirrored at the midline (blue and white dashed line) to produce the corresponding contralateral normal-appearing ROI (green), shown separately in panel **(c).** Axes are in [mm].

In the next step, the ROI of the central necrosis, if present, was manually outlined and subtracted from the tumor mask to obtain a mask of the solid tumor that did not include the central necrosis (cf. Figure 3).
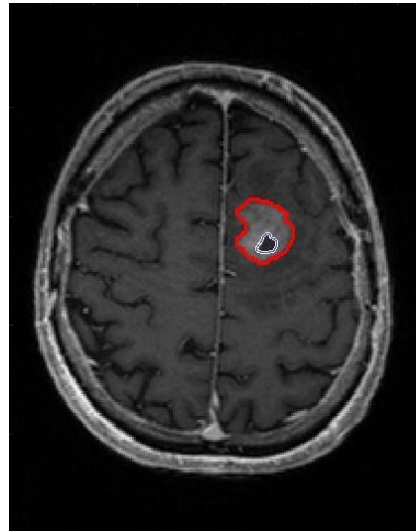
Figure 3: Axial T1-weighted contrast-enhanced image of a 71-year-old male glioblastoma patient. The red ROI marks contrast-enhancing tumor while the white/blue ROI inside the tumor indicates the central necrosis.

For an assessment of perfusion and oxygenation parameters in the peritumoral edematous area, a third, about 15mm to 20mm wide ROI was manually segmented in the peritumoral FLAIR hyperintensity on three consecutive T2-weighted FLAIR images with the largest peritumoral hyperintensity, leaving an approximately 3mm wide margin to avoid partial volume effects, as shown in Figure 4 (Dong et al., 2020). All ROIs were adapted to the tumor border, subtracting a cerebrospinal fluid (CSF) mask of ventricles and sulci generated automatically in SPM12. Therefore, ROIs in the FLAIR hyperintense area could sometimes be smaller than 15 mm or even incomplete (Blasel et al., 2010). The masks were audited by an experienced neuroradiologist from Mannheim University Medicine (Prof. Dr. Holger Wenz).
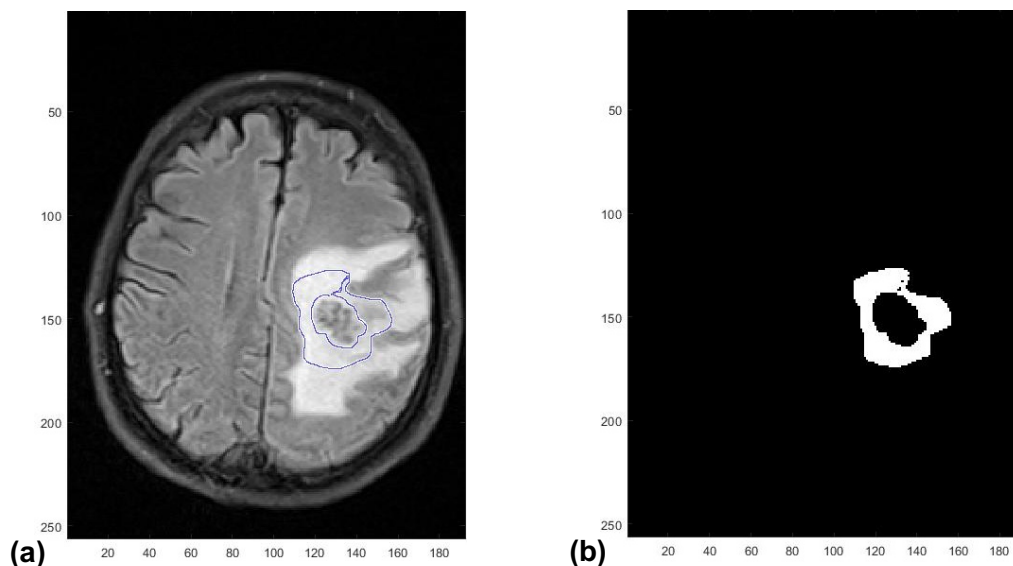
Figure 4: Axial FLAIR image of a 66-year-old male patient with a left parietal metastasis originating from an unknown primary cancer. The blue ROI shown in **(a)** marks the proximal edema bordering the contrast-enhancing tumor. The shape displayed in **(b)** is the extracted ROI mask. Axes are in [mm].

MATERIALS AND METHODS

2.4 Perfusion estimation

In order to estimate cerebral perfusion and blood volume, a quantitative perfusion map was created from the pCASL data using SPM12. CBF in ml/100g/min was calculated using the consensus recommendation for implementation of arterial spin-labeled perfusion MRI in clinical applications, jointly drawn up by the International Society for Magnetic Resonance in Medicine (ISMRM) Perfusion MR Study Group and the European ASL in Dementia consortium (Alsop et al., 2015):

$$\text{CBF} = \frac{6000 \cdot \lambda \cdot (SI_{\text{control}} - SI_{\text{label}}) \cdot e^{\frac{\text{PLD}}{T_{1\,\text{blood}}}}}{2\alpha \cdot T_{1\,\text{blood}} \cdot SI_{\text{PD}} \cdot (1 - e^{\frac{-\tau}{T_{1\,\text{blood}}}})} \quad , \tag{1}$$

where $\lambda = 0.9 \text{ml/g}$ is the blood-brain partition coefficient, SI_{control} and SI_{label} are the time-averaged signal intensities in the control and label images, respectively, $\text{PLD} = 2000 \text{ms}$ is the post-labeling delay, $T_{1\,\text{blood}} = 1650 \text{ms}$ at 3.0T is the longitudinal relaxation time of blood, $\alpha = 0.85$ is the labeling efficiency for pCASL, SI_{PD} is the signal intensity of a proton density-weighted image and $\tau = 1800 \text{ms}$ is the labeling duration (Hubertus, 2019). The factor 6000 converts from ml/g/s to ml/100g/min, as is the customary unit in literature. Time correction for multi-slice imaging was implemented to account for the different transit time of the labeled bolus depending on the time of slice acquisition (Alsop et al., 2015).

$CMRO_2$ in µmol/100g/min was calculated as follows:

$$\text{CMRO}_2 = \text{CBF} \cdot Y_a \cdot \text{OEF} \cdot [\text{H}] \quad , \tag{2}$$

where Y_a is the arterial oxygen saturation, assumed to be 98%, and [H] = 7.53µmol/ml is the heme molar concentration in tissue blood assuming a hematocrit of Hct = 0.357 in arterioles (Cho et al., 2018; Ma et al., 2020). OEF is calculated in Equation (3).

2.5 Oxygenation estimation

Based on the combined QSM + qBOLD approach, the mGRE data was used to estimate OEF:

$$\text{OEF} = 1 - \frac{Y}{Y_a} \quad , \tag{3}$$

where Y and Y_a are venous and arterial blood oxygenation, the latter again assumed to be 98% (Cho et al., 2018). Two methods were employed for combined QSM + qBOLD analysis of the mGRE data: an X-means machine learning-based clustering approach (Cho et al., 2020) and an artificial neural network (Hubertus et al., 2019b). The results from these two approaches were fed into a last fitting step by giving starting values for a quasi-Newton optimization: the limited-memory Broyden-Fletcher-Goldfarb-Shanno-Bound algorithm (Cho et al., 2020). The optimization was stopped once the relative change was smaller than 0.001 or a maximum of 50 iterations was reached (this was mostly the case after approx. 10 iterations).

MATERIALS AND METHODS

2.5.1 Artificial neural network

A feed-forward artificial neural network was used, designed in the Neural Network Toolbox in MATLAB R2017a (MathWorks, Natick, MA, USA). It consisted of one input layer, one hidden layer with 10 nodes and one output layer. The ANN has been described in detail in a previous study, where it was used to emulate the solution of the qBOLD model for free induction decay (Hubertus et al., 2019a):

$$S_{ANN}(Y, \nu, R_2, S_0, \chi_{nb}, t) = S_0 \cdot \exp\left(-\nu \cdot f(\delta\omega \cdot t) - R_2 \cdot t\right) \quad , \tag{4}$$

where Y is venous oxygen saturation, ν is deoxygenated blood volume, R_2 is the transverse relaxation rate, χ_{nb} is the non-blood susceptibility, S_0 is magnitude after excitation, $\delta\omega$ is the Lamor frequency shift due to the deoxygenated blood and t is time after excitation. In said study, the ANN was trained with 10^7 parameter sets containing random, normally distributed values for Y, ν, R_2, χ_{nb} and S_0. S_0 was calculated from Equation (4) so that the magnitude at the first time echo ($TE_1 = 4.5ms$) equaled 1. The mGRE signal decay was modeled for these parameter sets according to Equation (4) using t = 4.5ms. Gaussian noise was added to the resulting temporal signal to simulate a signal-to-noise ratio (SNR) of 100 at the first echo, similar to in-vivo data. The split between parameter sets used for training, validation and testing was 80%, 10% and 10%, respectively. Network weights were determined by minimizing the sum-of-squares error between network prediction and ground truth values with a Levenberg-Marquardt optimization. A schematic example of an artificial neural network with one hidden layer and an arbitrarily chosen number of nodes is shown in Figure 5.
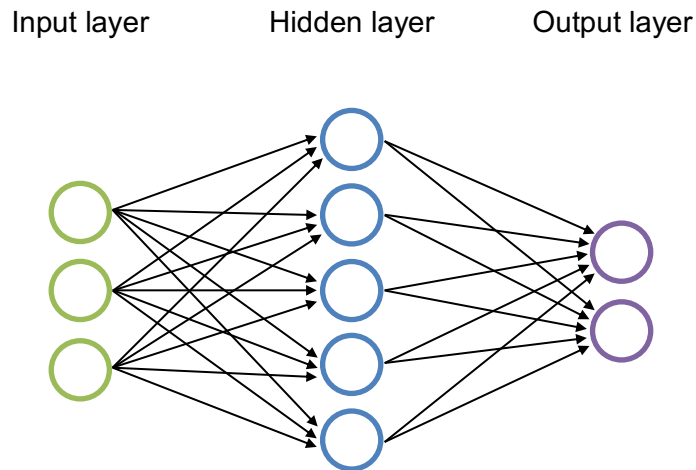
Figure 5   Schematic example of an artificial neural network with an input layer, one hidden layer and an output layer. The number of nodes in each layer does not represent the number of nodes chosen in this study.

The ANN used the normalized mGRE magnitude signal and the magnetic susceptibility from QSM (using the MEDI toolbox from the Cornell MRI Research Lab at Cornell University, New York, NY, USA) as inputs (Hubertus et al., 2019a). The outputs it returned were $(Y, R_2, \nu, \chi_{nb}, S_0/S(TE_1))^T$. After doing this for every voxel, OEF maps were created with Equation (3).

MATERIALS AND METHODS

2.5.2 X-means clustering

A machine learning-based clustering approach was used to group together voxels with similar magnitude decay over echoes. For this, a two-stage X-means method (Pelleg and Moore, 2000) was used to select the number of groups k: In a first step, the conventional k-means algorithm is employed for clustering, initialized with a given number of clusters $k = 1$. The Bayesian information criterion (BIC) measure is calculated and maximized to prevent overfitting (Hubertus, 2019). The BIC is the sum of the clustering log-likelihood and a penalty term on the number of clusters k. Goodness of fit (log-likelihood) increases with k, as does the risk of overfitting which is partly mitigated by including the penalty term on k in the BIC.

In the second step, the centroids (the point with the least sum of squared distances for all points in a cluster) of every cluster are replaced by two child centroids each. A local k-means with $k = 2$ is then performed within that cluster. In order to decide whether or not to keep the two child clusters, the BIC is computed. As long as BIC increases, the replacement is accepted. These two steps are iteratively looped until the overall BIC does not increase anymore or until k reaches a maximum value of 50 (Cho et al., 2020). A single value for Y, ν, χ_{nb} and R_2 was fitted per k-means group. The results of the initial groupwise fit were used as starting values for a k-means fit on all voxels. After the voxelwise fit, OEF maps were again created using Equation (3) (Hubertus et al., 2019a).

2.6 Statistical analysis

2.6.1 Oxygenation and perfusion in regions of interest

The statistical analyses were descriptive and performed in MATLAB R2020b. Variables were summarized using their median, minimum – maximum and interquartile range. For all patients, means and standard deviations of OEF, CBF and $CMRO_2$ were calculated in the ROIs set out in Figures 2 through 4. In patients with multiple cerebral metastases, perfusion and oxygenation parameters were not assessed on a metastasis-by-metastasis basis but averaged across all metastases present in the respective patient's brain. P-values < 0.05 were considered significant. A two-tailed Wilcoxon rank-sum test for independent samples was used to determine whether interindividual differences between glioblastomas and metastases were significant. A two-tailed Wilcoxon signed-rank test was used for intraindividual comparisons between CET and cNAB tissue and between CET and non-enhancing T2 FLAIR hyperintense peritumoral areas (NET2) to determine significant differences. Outliers were included in the statistical tests. Due to the explorative nature of this study, p-values were not adjusted for multiple tests and power analysis for determining the required sample size was not performed.

2.6.2 Receiver operating characteristic analysis

Receiver operating characteristic (ROC) analysis was performed to determine the best parameters for distinguishing glioblastomas from metastases. For this, a binary classifier support-vector machine (SVM) with a linear kernel was fitted to the following features: OEF, CBF and $CMRO_2$ in CET and NET2 as well as the ratio of these parameters in CET tissue divided by their respective counterparts in NET2 (Cortes and Vapnik, 1995; Server et al., 2011). Principal component analysis for exclusion of features that do not meaningfully contribute to explaining the variance of the data was not performed because of the small number of features included in the classification.

MATERIALS AND METHODS

OEF values emulated by the ANN, and not those calculated using the X-means clustering approach, were used for classification because the ANN values obtained in cNAB, assumed to be "healthy" brain, were much more in line with those in the abundant literature on MR and PET studies conducted on healthy volunteers and tumor patients (Fan et al., 2020; An and Lin, 2000; Lammertsma et al., 1983). For a detailed comparison between OEF values found in this study and those in the existing literature, please consult the discussion section.

Owing to the relatively small sample size of n = 15 patients, five-fold cross-validation was performed, calculating the mean error E as described by the following equation:

$$E = \frac{1}{K} \sum_{i=1}^{K} E_i \quad , \tag{5}$$

where K is the number of folds. For five-fold cross-validation, five folds are created with four of the five folds including the features of n/K patients each for training and the remaining observations being held out for validation. True error is calculated as the average error rate from all K folds. This was iterated 10 times for every feature that was evaluated. Accuracy and ROC data were calculated and averaged over all iterations (Swinburne et al., 2019).

In order to compare the performance of the linear kernel SVM to that of different classifiers, a 5-fold cross-validated multivariable training run across a number of different classifier algorithms including weighted k-nearest neighbor (KNN), decision trees, logistic regression, Naïve Bayes as well as quadratic kernel SVM and Gaussian SVM was performed in the MATLAB R2020b Classification Learner toolbox. For this purpose, the two features OEF_{CET} and $CMRO_{2\ CET/NET2}$ that previously yielded the best classification accuracy with a linear kernel SVM were used.

3 RESULTS

In following section, the findings of this study are presented, beginning with OEF and CBF maps that were generated using the QSM + qBOLD model and the pCASL images (cf. Figure 6 and Figure 7). OEF, CBF and $CMRO_2$ are first compared in the contrast-enhancing tumor ROI between glioblastoma and metastasis patients and, in a second step, between contrast-enhancing tumor and contralateral normal-appearing brain tissue. In an additional step, the very same oxygenation and perfusion parameters are shown for the non-enhancing T2 FLAIR hyperintense peritumoral area and a comparison is drawn to contrast-enhancing tumor.

The two distinct approaches used in this study yielded different estimates for OEF and, due to the linear dependency of the two parameters, $CMRO_2$. They are displayed in this section: firstly, the artificial neural network and secondly, the X-means clustering method. The results of these methods are compared and significant differences highlighted. Tables A1 and A2 in the appendix give OEF, CBF and $CMRO_2$ values for each of the 15 patients included in the study, broken down by tumor entity and separately for the ANN and clustering approach.

Finally, results from the receiver operating characteristic analysis are highlighted that was performed as a means to determine the optimal features for distinguishing glioblastoma from cerebral metastasis using oxygenation and perfusion parameters.

3.1 Oxygenation and perfusion maps

The OEF maps of a 54-year-old female patient with left occipito-temporal glioblastoma that are supplied in Figure 6 serve as an example for visual comparison of X-means clustering and ANN results. Part of the tumor in the left hemisphere is visible displaying a higher OEF than the tissue surrounding it. The ANN shows higher estimated OEF values across the brain while clustering appears to yield generally lower OEF, a distinction between grey and white matter is not possible with either of the methods.
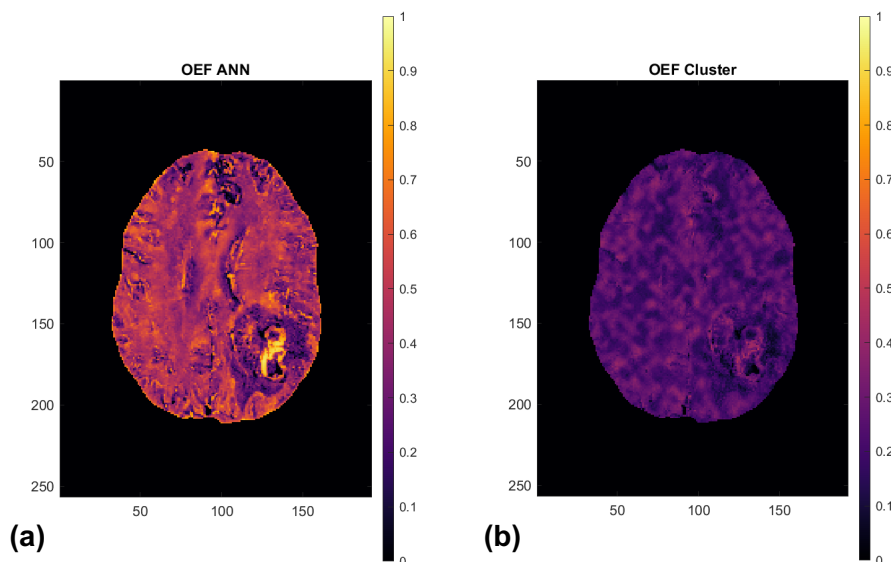
Figure 6: OEF maps of a 54-year-old female patient with left occipito-temporal glioblastoma. Axes are in mm. The scales to the right of each of the two images give OEF (e.g. 0.5 = 50%). **(a)** The OEF map is displayed as calculated with the ANN method, **(b)** shows an OEF map emulated with X-means clustering.

RESULTS

The CBF and $CMRO_2$ maps shown in Figure 7 give an illustrative overview of CBF calculated in SPM as well as ANN and X-means clustering results for $CMRO_2$ for a different, 71-year-old glioblastoma patient.
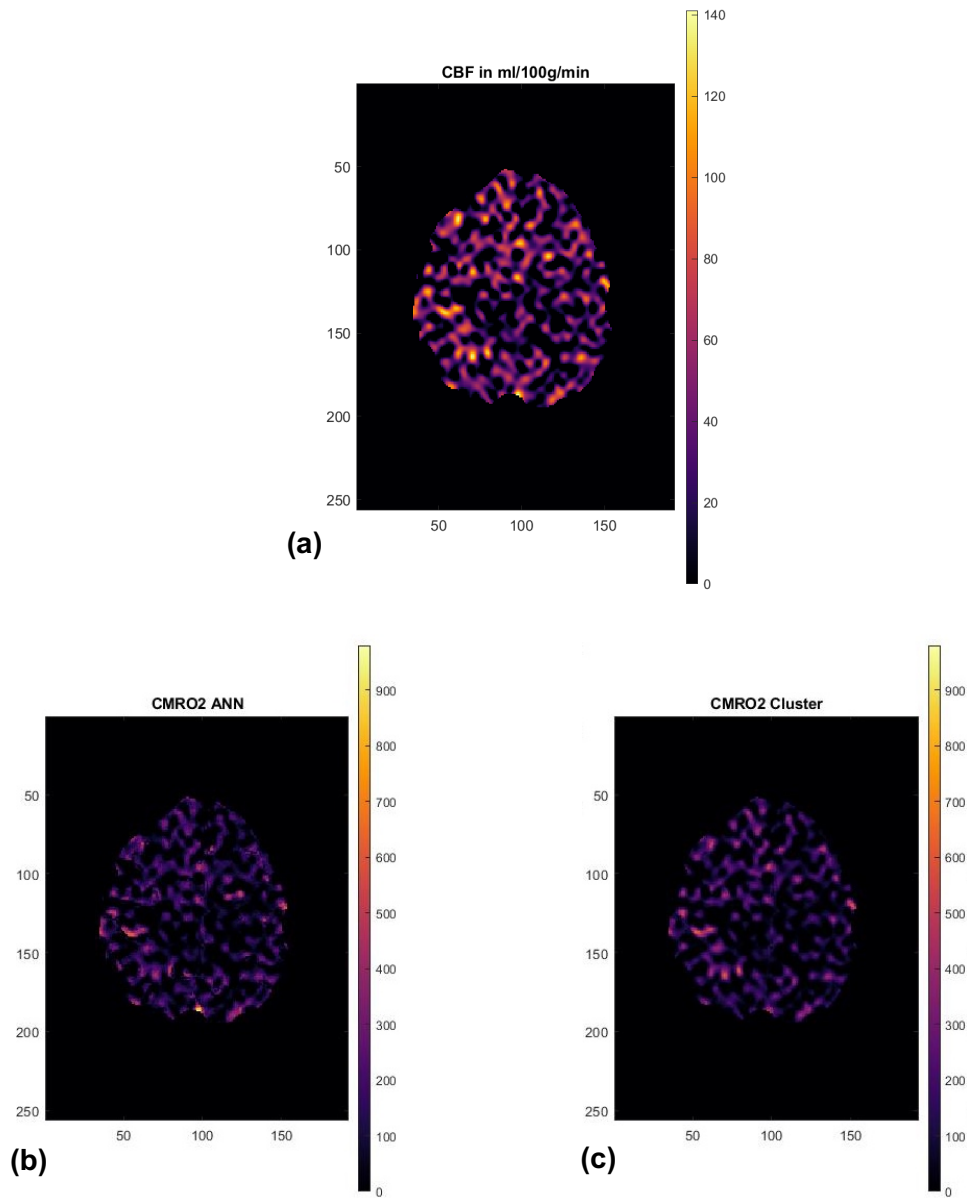
Figure 7:   Perfusion and oxygenation maps of a 71-year-old male glioblastoma patient. **(a)** The image shows a perfusion map with CBF in ml/100g/min. **(b)** $CMRO_2$ map showing results from the ANN in µmol/100g/min. **(c)** $CMRO_2$ map derived from X-means clustering results in µmol/100g/min. Axes are in mm.

RESULTS

3.2 Tissue oxygenation and perfusion in CET and cNAB

3.2.1 Artificial neural network results

Table 1 lists means and standard deviations for OEF, CBF and $CMRO_2$ in CET and cNAB tissue. Average values across patient groups are shown in order to compare glioblastoma to brain metastasis patients. OEF was calculated using the ANN method. Significant differences in OEF were found between CET of glioblastomas and metastases ($36.2 \pm 4.9\%$ versus $43.9 \pm 7.0\%$). For glioblastomas, the difference between OEF in CET and in cNAB tissue was also significant ($36.2 \pm 4.9\%$ versus $42.8 \pm 4.4\%$). CBF values were significantly higher in contrast-enhancing glioblastoma tissue than they are in cNAB (50.8 ± 23.1 versus 39.5 ± 26.7ml/100g/min). The same applies to CBF in metastases when compared to cNAB (54.9 ± 22.4 versus 31.8 ± 12.4ml/100g/min). For $CMRO_2$, cNAB showed significantly lower values than CET in metastasis patients only (182.6 ± 104.6 versus 108.3 ± 36.7µmol/100g/min). No significant differences were found between glioblastomas and metastases for CBF and $CMRO_2$.

Table 1: Overview of means and standard deviations of oxygen extraction fraction (OEF), cerebral blood flow (CBF) and cerebral metabolic rate of oxygen ($CMRO_2$) in glioblastoma and metastasis patients, for contrast-enhancing tumor (CET) and contralateral normal-appearing brain tissue (cNAB). OEF was calculated using the artificial neural network (ANN) approach. *P*-values were obtained using Wilcoxon rank-sum test for comparisons between glioblastomas and metastases and Wilcoxon signed-rank test for intraindividual comparisons between CET and cNAB tissue to determine significant ($p < 0.05$, bold font) differences.

ANN	CET	cNAB	*p*
	OEF [%]		
Glioblastomas	36.2 ± 4.9	42.8 ± 4.4	**0.02**
Metastases	43.9 ± 7.0	47.9 ± 8.1	0.44
p	**0.03**	0.27	
	CBF [ml/ 100g/ min]		
Glioblastomas	50.8 ± 23.1	39.5 ± 26.7	**0.03**
Metastases	54.9 ± 22.4	31.8 ± 12.4	**0.01**
p	0.33	0.95	
	CMRO2 [µmol/ 100g/ min]		
Glioblastomas	142.5 ± 77.3	131.7 ± 107.8	0.45
Metastases	182.6 ± 104.6	108.3 ± 36.7	**0.01**
p	0.15	0.60	

An overview of OEF, CBF and CMRO$_2$ in glioblastomas and metastases as well as their corresponding contralateral normal-appearing correlates is given in Figure 8. OEF, as determined with the ANN approach, was significantly lower (p = 0.02) in the contrast-enhancing part of glioblastomas when compared to cNAB. CBF was significantly higher in CET than in cNAB, both in glioblastoma (p = 0.03) and metastasis (p = 0.01) patients. The net effect on CMRO$_2$ was positive: CMRO$_2$ was higher in CET than in cNAB, with the difference being significant only for metastases (p = 0.01). The respective parameters in CET and cNAB tissue are displayed in Table 1.
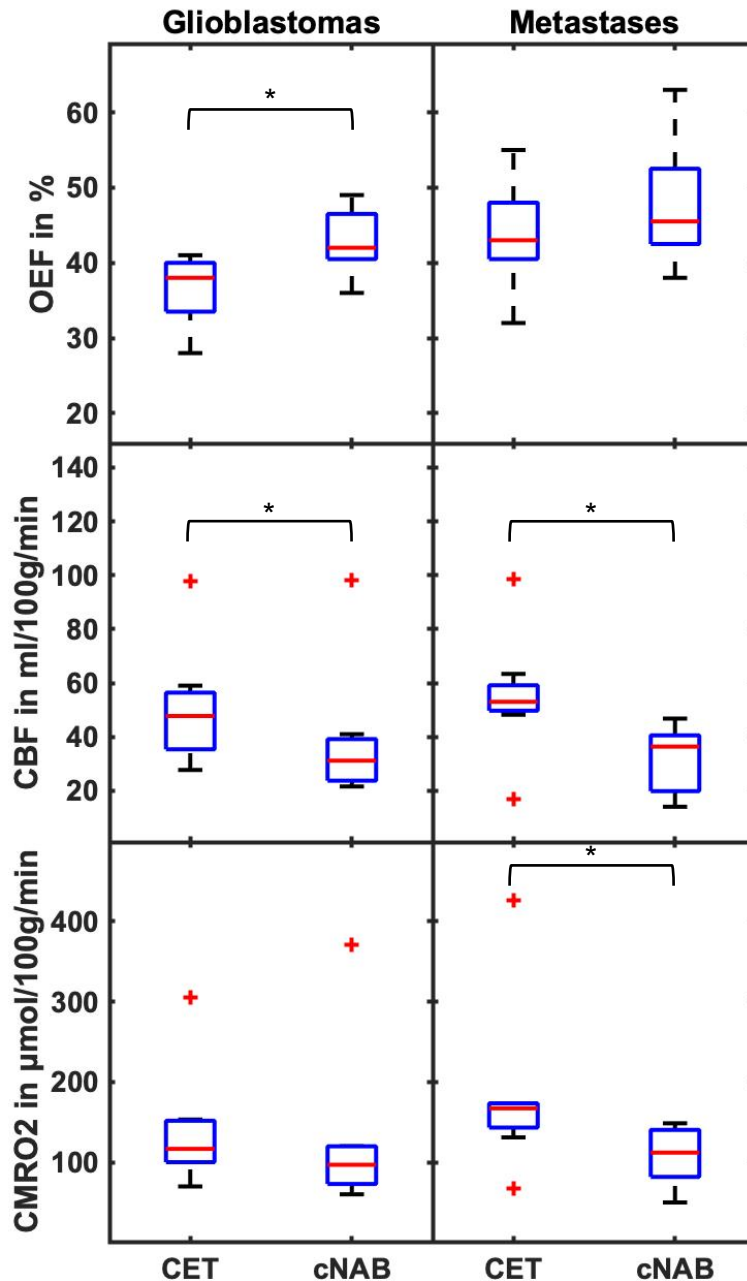
Figure 8: Boxplots comparing oxygen extraction fraction (OEF), cerebral blood flow (CBF) and cerebral metabolic rate of oxygen (CMRO$_2$) in the contrast-enhancing tumor (CET) region to contralateral normal-appearing brain tissue (cNAB). Results for both glioblastomas and metastases are shown. OEF was computed using the artificial neural network (ANN) method. The median is depicted in red, the first and third quartile are blue and the black whiskers indicate 1.5 times the interquartile distance or the maximum/minimum value, if contained within that distance. Outliers are displayed as red crosses. Significant differences (p < 0.05) between CET and cNAB tissue are marked with an asterisk.

RESULTS

Figure 9 shows a comparison between glioblastomas and metastases in terms of OEF, CBF and CMRO$_2$ in CET. OEF, as determined by the ANN, was significantly lower ($p = 0.03$) in glioblastomas than it was in metastases. CBF and CMRO$_2$ did not significantly differ. Means and standard deviations for the respective values in glioblastoma and metastasis patients are shown in the "CET" column of Table 1. In each of the two groups, one positive outlier for CBF (and therefore also for CMRO$_2$) is displayed as a red cross.
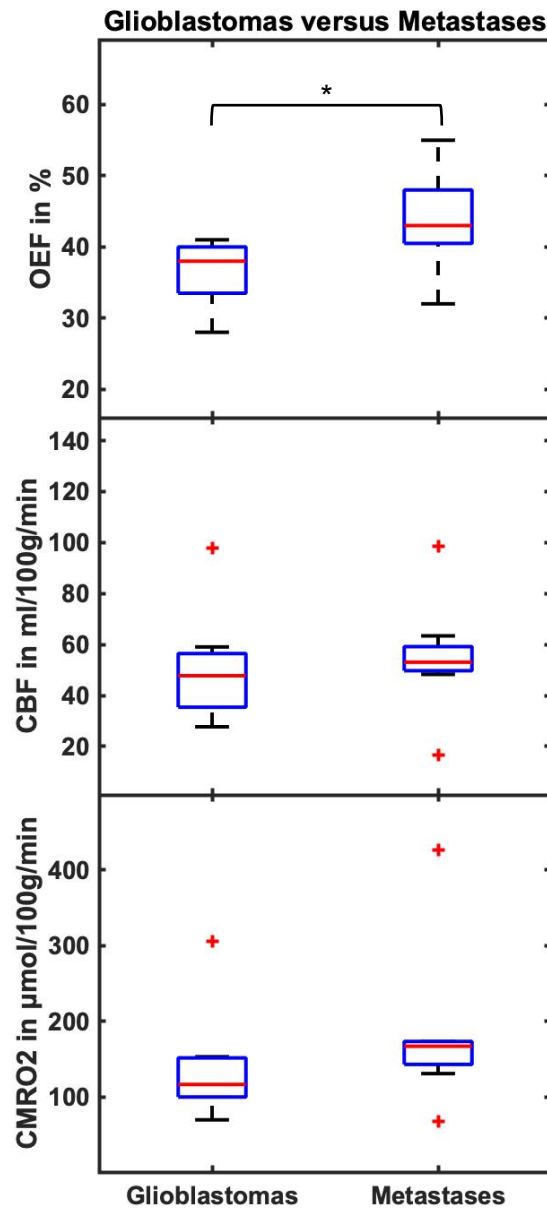
Figure 9: Boxplots illustrating oxygen extraction fraction (OEF), cerebral blood flow (CBF) and cerebral metabolic rate of oxygen (CMRO$_2$) in the contrast-enhancing tumor ROI in glioblastomas and cerebral metastases. OEF was computed using the artificial neural network (ANN) method. The median is depicted in red, the first and third quartile are blue and the black whiskers indicate 1.5 times the interquartile distance or the maximum/minimum value, if contained within that distance. Outliers are displayed as red crosses. The significant difference ($p < 0.05$) between glioblastomas and metastases is marked with an asterisk.

3.2.2 X-means clustering results

Table 2 lists means and standard deviations for OEF, CBF and CMRO$_2$ in tumor and cNAB tissue. Average values across patient groups are shown in order to compare glioblastoma to brain metastasis patients. OEF was calculated using the clustering method. The differences in OEF between glioblastomas and metastases and between CET and cNAB were not significant. However, CBF values were significantly higher in tumor tissue when compared to cNAB tissue, both for glioblastomas and metastases (the same CBF data as in Table 1 is presented here since CBF is calculated using SPM12 and does not differ between the ANN and clustering approach). For CMRO$_2$, cNAB showed significantly lower values when compared to CET in metastasis patients only (156.9 $\pm$ 88.9 versus 85.8 $\pm$ 39.3μmol/100g/min). No significant differences were found between glioblastomas and metastases for CBF and CMRO$_2$.

Table 2: Overview of means and standard deviations of oxygen extraction fraction (OEF), cerebral blood flow (CBF) and cerebral metabolic rate of oxygen (CMRO$_2$) in glioblastoma and metastasis patients, for contrast-enhancing tumor (CET) and contralateral normal-appearing brain tissue (cNAB). OEF was calculated using the clustering approach. P-values were obtained using Wilcoxon rank-sum test for comparisons between glioblastomas and metastases and Wilcoxon signed-rank test for intraindividual comparisons between CET and cNAB tissue to determine significant ($p < 0.05$, bold font) differences.

Cluster	CET	cNAB	p
	OEF [%]		
Glioblastomas	29.2 ± 5.3	30.7 ± 4.1	0.20
Metastases	33.1 ± 5.9	32.3 ± 6.6	0.73
p	0.22	0.45	
	CBF [ml/ 100g/ min]		
Glioblastomas	50.8 ± 23.1	39.5 ± 26.7	**0.03**
Metastases	54.9 ± 22.4	31.8 ± 12.4	**0.01**
p	0.33	0.95	
	CMRO2 [μmol/ 100g/ min]		
Glioblastomas	131.0 ± 65.5	105.3 ± 72.3	0.05
Metastases	156.9 ± 88.9	85.8 ± 39.3	**0.01**
p	0.27	0.86	

RESULTS

An overview of OEF, CBF and CMRO$_2$ in glioblastomas and metastases as well as their corresponding contralateral normal-appearing correlates is given in Figure 10. OEF, as determined with the clustering approach, did not significantly differ between CET and cNAB in either of the two groups. CBF was found to be significantly higher in CET than in cNAB for glioblastomas (p = 0.03) and for metastases (p = 0.01) and CMRO$_2$ was significantly higher (p = 0.01) in CET than in cNAB in metastasis patients only. Means and standard deviations for the respective parameters in tumor tissue and cNAB are shown in Table 2.
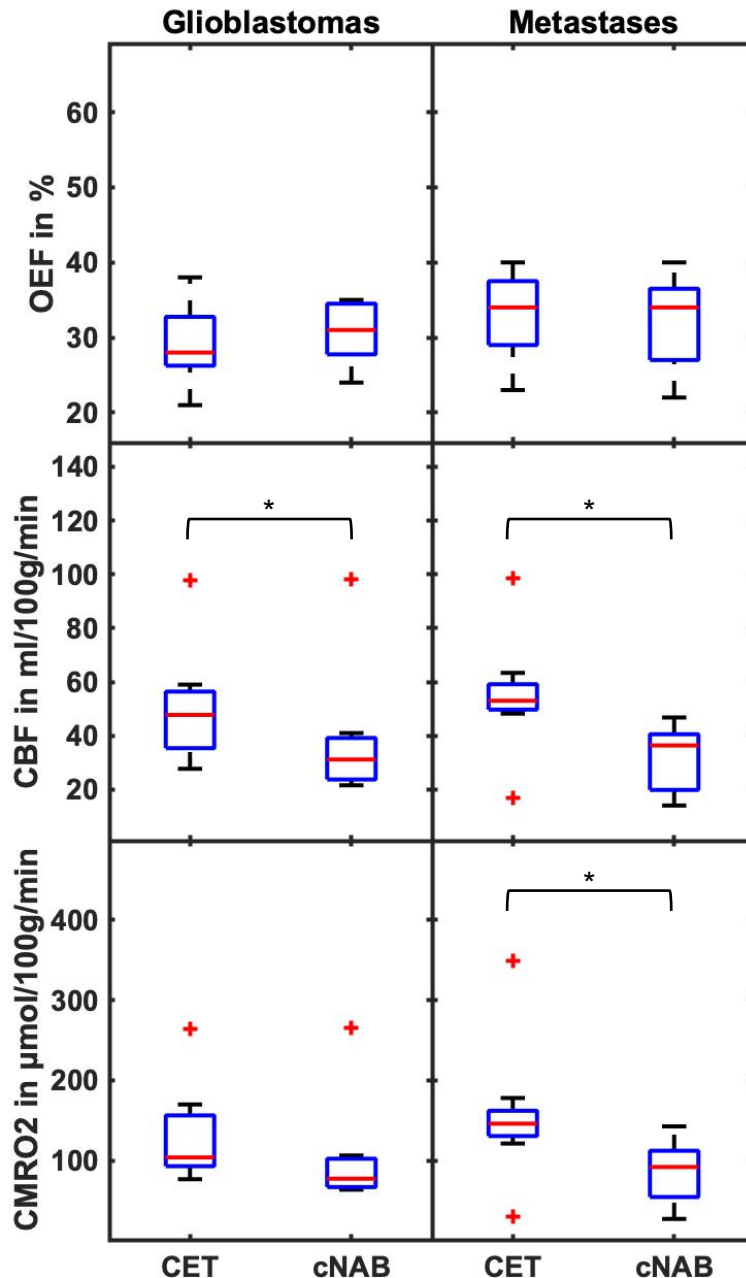
Figure 10: Boxplots comparing oxygen extraction fraction (OEF) and cerebral metabolic rate of oxygen (CMRO$_2$) in the contrast-enhancing tumor (CET) region to contralateral normal-appearing brain tissue (cNAB). Results for both glioblastomas and metastases are displayed. OEF was computed using the clustering method. The median is depicted in red, the first and third quartile are blue and the black whiskers indicate 1.5 times the interquartile distance or the maximum/minimum value, if contained within that distance. Outliers are displayed as red crosses. Significant differences (p < 0.05) between CET and cNAB tissue are marked with an asterisk.

Glioblastomas and metastases are compared in terms of their respective OEF, CBF and CMRO$_2$ in Figure 11. OEF, as determined with clustering, CBF and CMRO$_2$ were not significantly different in glioblastomas and metastases. In each of the two groups, one positive outlier for CBF (and therefore also for CMRO$_2$) is displayed as a red cross. Means and standard deviations for the respective values in glioblastoma and metastasis patients are shown in the "CET" column of Table 2.
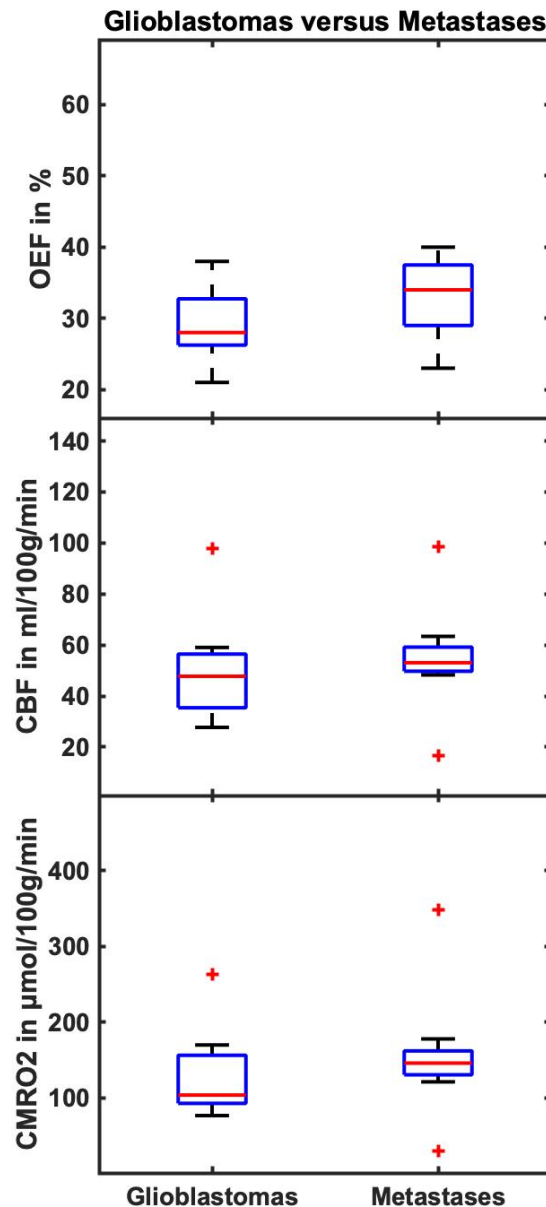
Figure 11: Boxplots illustrating oxygen extraction fraction (OEF), cerebral blood flow (CBF) and cerebral metabolic rate of oxygen (CMRO$_2$) in the contrast-enhancing tumor ROI of glioblastomas and cerebral metastases. OEF was computed using the clustering method. The median is depicted in red, the first and third quartile are blue and the black whiskers indicate 1.5 times the interquartile distance or the maximum/minimum value, if contained within that distance. Outliers are displayed as red crosses.

3.3 Perfusion and oxygenation parameters in the peritumoral region

A comparison of means and standard deviations for oxygenation and perfusion parameters in CET and in NET2 is shown in Table 3. Averages were calculated across patient groups for glioblastomas and cerebral metastases. Both ANN and X-means clustering approach results are displayed for OEF and $CMRO_2$. While there were no significant differences between glioblastomas and metastases and between CET and NET2 ROIs in glioblastoma patients, all differences displayed between the CET and the NET2 region for the cerebral metastasis group were significant. This applies for results computed with the ANN as well as with the clustering approach.

Table 3: Overview of means and standard deviations of oxygen extraction fraction (OEF), cerebral blood flow (CBF) and cerebral metabolic rate of oxygen ($CMRO_2$) in glioblastoma and metastasis patients, for contrast-enhancing tumor (CET) and non-enhancing T2 FLAIR hyperintense peritumoral region (NET2). OEF and $CMRO_2$ calculated using the ANN and the clustering approach are supplied. *P*-values were obtained using Wilcoxon rank-sum test for comparisons between glioblastomas and metastases and Wilcoxon signed-rank test for intraindividual comparisons between CET and NET2 ROIs to determine significant ($p < 0.05$, bold font) differences.

ANN	CET	NET2	*p*
	OEF [%]		
Glioblastomas	36.2 ± 4.9	30.3 ± 9.6	0.11
Metastases	43.9 ± 7.0	28.3 ± 6.6	**0.01**
p	**0.03**	0.95	

Cluster	OEF [%]		*p*
Glioblastomas	29.2 ± 5.3	25.9 ± 10.2	0.27
Metastases	33.1 ± 5.9	22.8 ± 7.1	**0.01**
p	0.22	0.52	

	CBF [ml/ 100g/ min]		*p*
Glioblastomas	50.8 ± 23.1	36.5 ± 32.5	0.15
Metastases	54.9 ± 22.4	15.4 ± 10.9	**0.01**
p	0.33	0.18	

ANN	CMRO2 [μmol/ 100g/ min]		*p*
Glioblastomas	142.5 ± 77.3	84.0 ± 77.0	0.08
Metastases	182.6 ± 104.6	30.7 ± 15.2	**0.01**
p	0.15	0.18	

Cluster	CMRO2 [μmol/ 100g/ min]		*p*
Glioblastomas	131.0 ± 65.5	95.4 ± 107.4	0.27
Metastases	156.9 ± 88.9	31.9 ± 26.7	**0.01**
p	0.27	0.15	

A visual representation of the results described above and shown in Table 3 is supplied in Figure 12. It highlights that the differences in tissue oxygenation and perfusion between enhancing tumor and NET2 ROIs were only significant for metastasis patients. All parameters in metastasis patients, i.e. OEF, CBF and $CMRO_2$, were significantly higher ($p = 0.01$) in the CET region of interest than in the peritumoral NET2 region. Meanwhile, for the glioblastoma group, neither the difference in OEF nor CBF, nor $CMRO_2$ was significant.
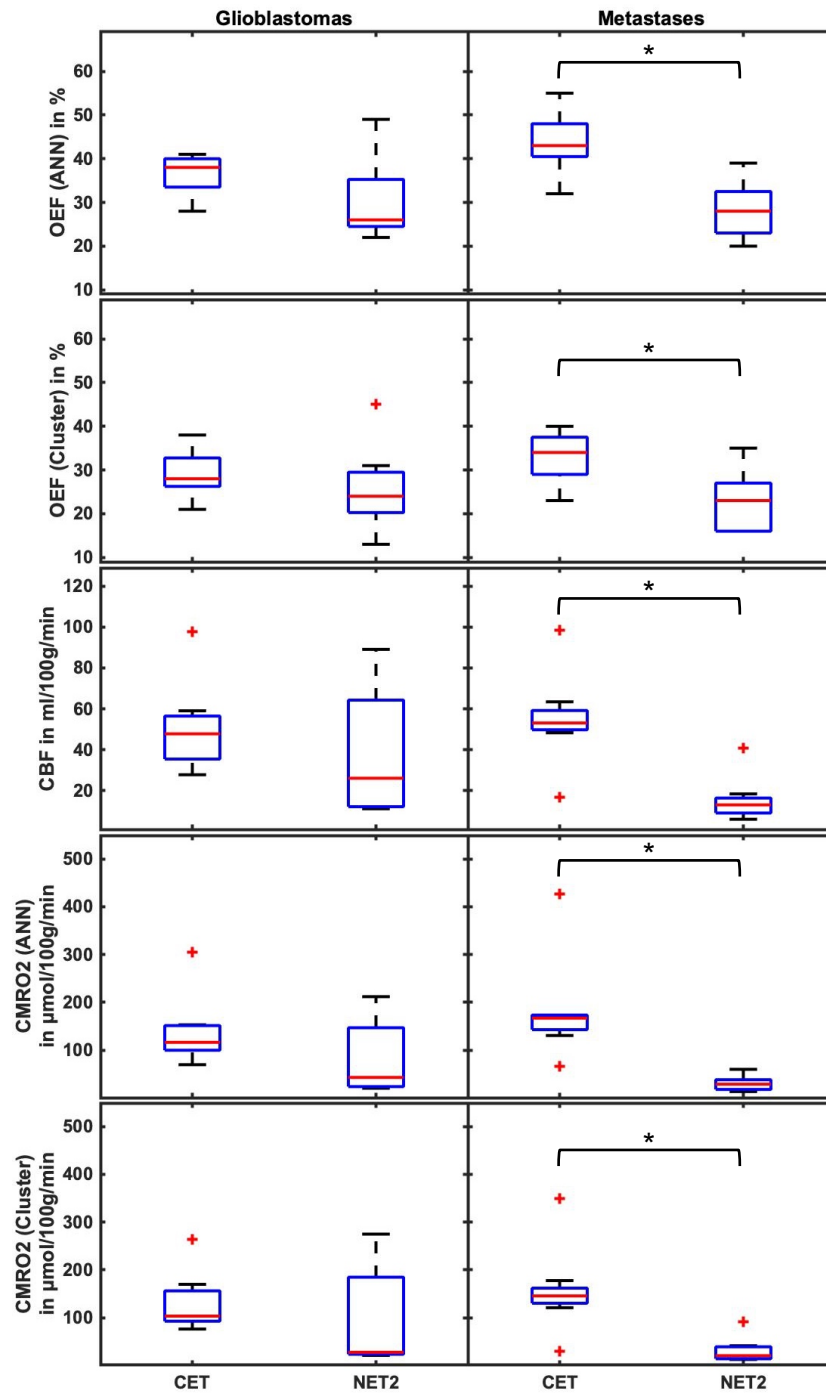
Figure 12: Boxplots comparing oxygen extraction fraction (OEF), cerebral blood flow (CBF) and cerebral metabolic rate of oxygen (CMRO$_2$) in the contrast-enhancing tumor (CET) region with peritumoral non-enhancing T2 FLAIR hyperintense region (NET2). Results for both glioblastomas and metastases are displayed. The median is depicted in red, the first and third quartile are blue and the black whiskers indicate 1.5 times the interquartile distance or the maximum/minimum value, if contained within that distance. Outliers are displayed as red crosses. Significant differences ($p < 0.05$) between CET and cNAB tissue are marked with an asterisk.

A metric for differentiation of glioblastomas and metastases is the ratio of oxygenation and perfusion parameters within CET divided by NET2. A boxplot depicting these ratios for OEF, CBF and CMRO$_2$ is displayed in Figure 13. It shows that, while OEF for CET/NET2 was not significantly different between glioblastoma and metastasis patients, the ratio for CBF was significantly higher (p = 0.04) for metastases, as was the ratio for CMRO$_2$ (p = 0.01).
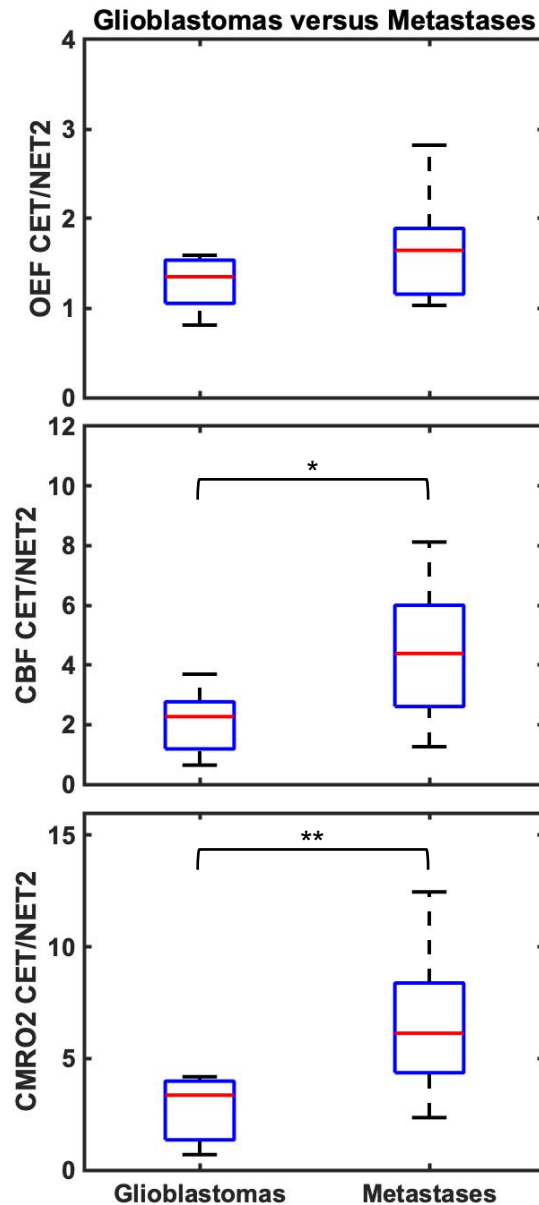
Figure 13: Boxplots showing the ratios of oxygen extraction fraction (OEF), cerebral blood flow (CBF) and cerebral metabolic rate of oxygen (CMRO2) in the contrast-enhancing tumor (CET) ROI divided by the peritumoral non-enhancing T2 FLAIR hyperintense (NET2) ROI for glioblastoma and cerebral metastasis patients. OEF was computed using the artificial neural network (ANN) method. The median is depicted in red, the first and third quartile are blue and the black whiskers indicate 1.5 times the interquartile distance or the maximum/minimum value, if contained therein. The significant difference (p = 0.04) is marked with an asterisk, the highly significant difference (p = 0.01) is marked with two asterisks.

3.4 Comparison of ANN and X-means clustering results

A comparison between ANN and clustering results for OEF and $CMRO_2$ in CET of glioblastomas and metastases can be found in Figure 14. The method used for calculation of each value is indicated by a subscript "ANN" or "Cluster". Means and standard deviations for glioblastoma were OEF_{ANN} = 36.2 ± 4.9%, $OEF_{Cluster}$ = 29.2 ± 5.3%, $CMRO_{2\,ANN}$ = 142.5 ± 77.3µmol/100g/min and $CMRO_{2\,Cluster}$ = 131.0 ± 65.5µmol/100g/min. Likewise, metastases showed OEF_{ANN} = 43.9 ± 7.0%, $OEF_{Cluster}$ = 33.1 ± 5.9%, $CMRO_{2\,ANN}$ = 182.6 ± 104.6µmol/100g/min and $CMRO_{2\,Cluster}$ = 156.9 ± 88.9µmol/100g/min. OEF obtained using the ANN approach was significantly higher than that calculated with the clustering approach both for glioblastomas (p = 0.02) and for metastases (p = 0.02). $CMRO_2$ showed no significant differences.
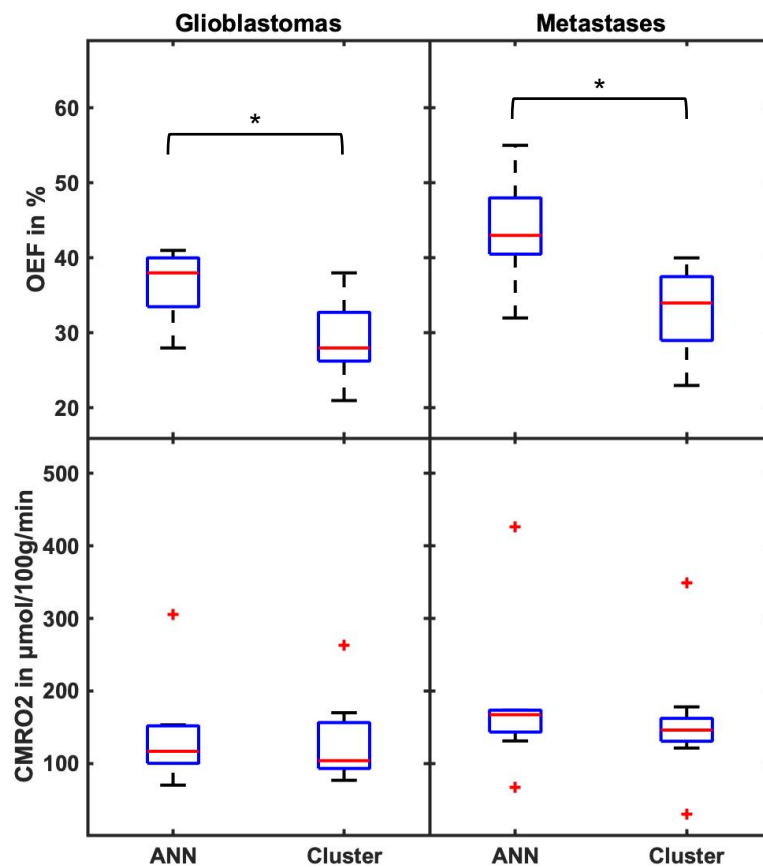

Figure 14: Boxplot comparing oxygen extraction fraction (OEF) and cerebral metabolic rate of oxygen ($CMRO_2$) in the contrast-enhancing tumor ROI of glioblastoma and metastasis patients. Results of both the artificial neural network (ANN) and the clustering approach are displayed. The median is depicted in red, the first and third quartile are blue and the black whiskers indicate 1.5 times the interquartile distance or the maximum/minimum value, if contained within that distance. Outliers are displayed as red crosses. Significant differences ($p < 0.05$) between the two methods are marked with an asterisk.

RESULTS

The average values for OEF in CET differed by 9 percentage points between ANN and X-means clustering with a mean of 40.3 and 31.3%, respectively. This difference was a little less pronounced in glioblastomas (36.2 versus 29.2%) than in cerebral metastases (43.9 versus 33.1%). In cNAB, the gap between the two methods was larger: OEF had a mean of 45.5% across all tumors with the ANN compared to 31.6% with clustering, glioblastomas again showing not as large a difference (42.8 versus 31.6%) as the metastasis group (47.9 versus 32.3%). For the peritumoral region that was analyzed, NET2, the differences were less pronounced: Averaged across all patients, the ANN method yielded an OEF of 29.2% in NET2 while X-means clustering showed an OEF of 24.2%. Neither the glioblastoma (30.3 versus 25.9%) nor the cerebral metastasis group (28.3 versus 22.8%) showed very wide spreads.

$CMRO_2$ in CET displayed higher mean values with the ANN method than with clustering (163.9 versus 144.8µmol/100g/min), albeit not as distinct as in OEF. This is due to the fact that the CBF values for calculation of $CMRO_2$ were identical in both approaches since they are estimated in SPM based on the pCASL images. Once more, this difference was more pronounced for cerebral metastases (182.6 versus 156.9µmol/100g/min) than for glioblastomas (142.5 versus 131.0µmol/100g/ min). $CMRO_2$ in cNAB showed a similar trend, yielding 119.3 from ANN versus 94.9µmol/100g/min from clustering across both tumor groups. This time, though, the difference was greater in glioblastoma (131.7 versus 105.3µmol/100g/min) than in cerebral metastasis patients (108.3 versus 85.8µmol/100g/ min). $CMRO_2$ in NET2 was different in that it was the only metric for which the clustering approach yielded higher values than the ANN method. Across all patients, $CMRO_2$, as determined by the ANN, was 55.6µmol/100g/min while clustering came out at 61.5µmol/100g/min. This held true for glioblastomas (84.0 versus 95.4µmol/100g/min) and for metastases (30.7 versus 31.9µmol/100g/min).

RESULTS

The Bland-Altman plots in Figure 15 serve as a visual comparison of ANN and X-means clustering results. Inspection shows OEF in glioblastomas to be generally lower than in metastases (upper plot), whereas $CMRO_2$ does not show any such trend (lower plot). ANN results were higher than clustering results for OEF and $CMRO_2$ but the mean difference for both parameters was compatible with 0 within a band of $\pm$ 1.96 standard deviations.
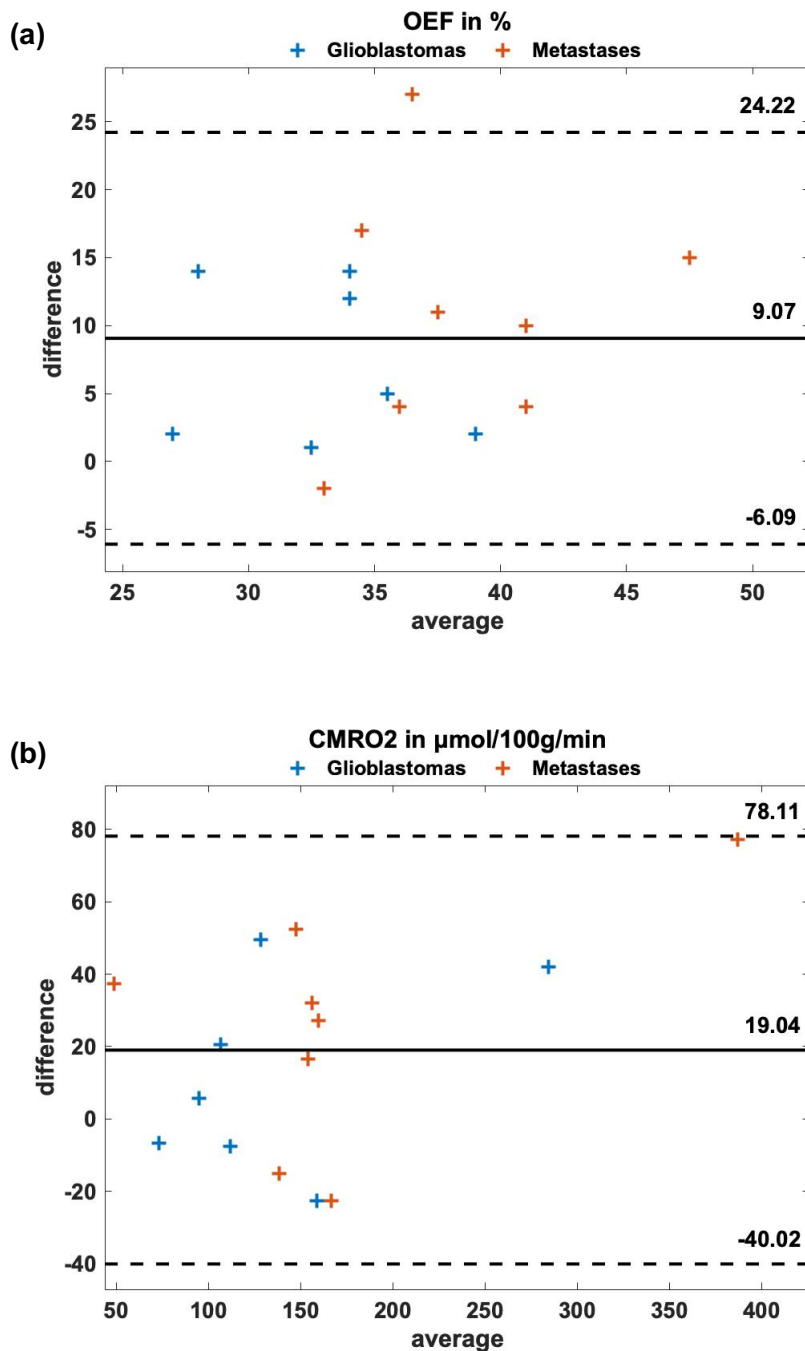
Figure 15: Bland-Altman plots showing a comparison of results of the artificial neural network (ANN) and the clustering approach for **(a)** oxygen extraction fraction (OEF) and **(b)** cerebral metabolic rate of oxygen ($CMRO_2$) within the contrast-enhancing tumor ROI of glioblastomas (blue crosses) and metastases (orange crosses). Depicted are the difference between ANN and X-means clustering ($x_{ANN} - x_{Cluster}$) and the average ($x_{ANN} + x_{Cluster}$) / 2), mean difference (solid black line) and mean difference $\pm$ 1.96 · standard deviation (dashed black lines).

3.5 ROC analysis for binary classification using a support-vector machine

After fitting a classifier SVM to a number of features outlined in section 2.6.2, different metrics for binary classification of glioblastomas and metastases were assessed. The ROC curves of the ratios of OEF, CBF and $CMRO_2$ in tumor divided by peritumoral NET2 region are exhibited in Figure 16 ($OEF_{CET/NET2}$, $CBF_{CET/NET2}$ and $CMRO_{2\ CET/NET2}$). The best combination of two or more features in terms of the area under the curve (AUC) is also displayed, fitting the SVM to OEF_{CET} + $CMRO_{2\ CET/NET2}$. Two more ROC curves (Figure A1 and Figure A2) with results for the same oxygenation and perfusion parameters in the CET and the NET2 ROI can be found in the appendix in section 7.2.
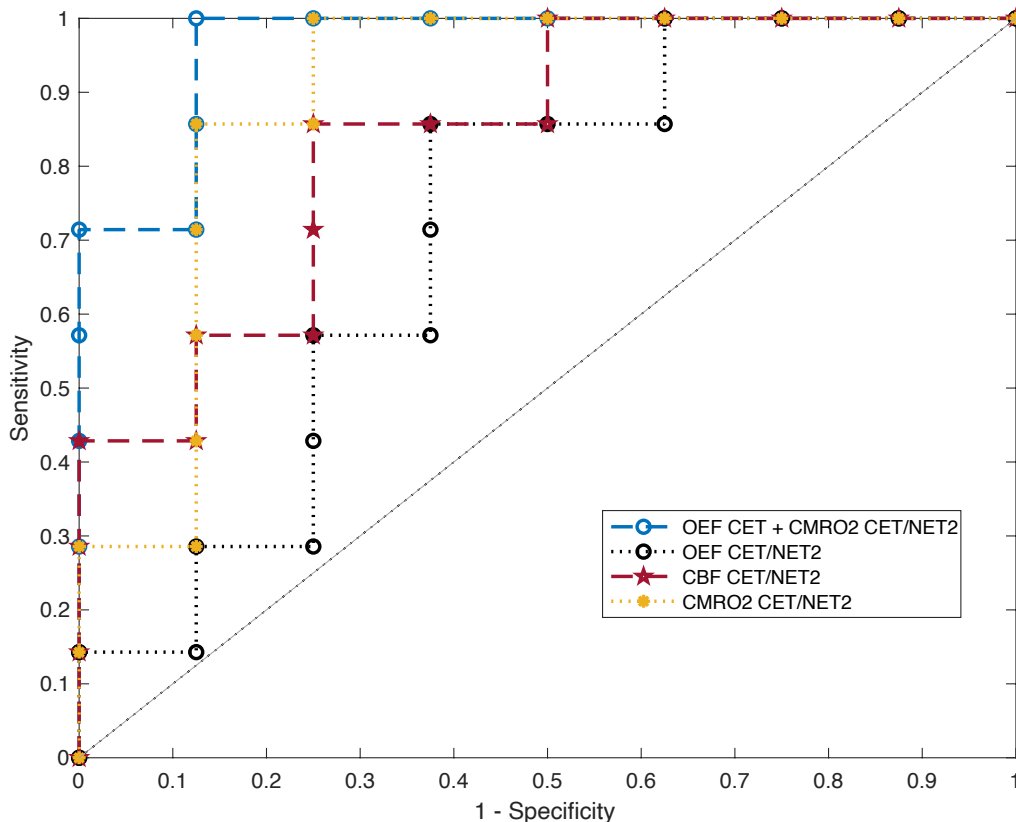
Figure 16: Five-fold cross-validated receiver operating characteristic (ROC) curves for the support-vector machine classifier predicting binary outcome (glioblastoma or metastasis). Curves are shown for the ratios of oxygen extraction fraction ($OEF_{CET/NET2}$, black dashed line), cerebral blood flow ($CBF_{CET/NET2}$, red dashed line) and cerebral metabolic rate of oxygen ($CMRO_{2\ CET/NET2}$, yellow dashed line) in contrast-enhancing tumor (CET) divided by peritumoral non-enhancing T2 FLAIR hyperintensity (NET2) as well as for the multivariable fit to OEF_{CET} + $CMRO_{2\ CET/NET2}$ (blue dashed line). OEF_{CET}: OEF in contrast-enhancing tumor.

A performance comparison of different classification algorithms can also be found in the appendix in section 7.2, where the ROC curves of k-nearest neighbor, decision trees, logistic regression, Naïve Bayes as well as quadratic kernel SVM and Gaussian SVM are shown for the multivariable classification problem with the two features OEF_{CET} + $CMRO_{2\ CET/NET2}$.

RESULTS

For each parameter, values for accuracy, optimal sensitivity and specificity and AUC were calculated and are listed in Table 4. $CMRO_{2\,CET/NET2}$ emerged as the best single feature for differentiation of glioblastoma from metastases. The resulting model had an AUC of 0.85 with an accuracy of 83% at an optimal sensitivity and specificity of 85% and 82% respectively. The next best single classification features in terms of AUC were the ratio $CBF_{CET/NET2}$ (0.80) and OEF in enhancing tumor (0.79). The highest multivariable AUC was achieved when fitting the SVM to the two features OEF_{CET} + $CMRO_{2\,CET/NET2}$ (0.94), allowing for an accurate classification of the tumors in 93% of cases, with a sensitivity of 99% and a specificity of 88%.

Table 4:   ROC analysis of different oxygenation and perfusion markers in T1 contrast-enhancing tumor (CET), peritumoral non-enhancing T2 FLAIR hyperintensity (NET2) and their ratios (CET/NET2). OEF: oxygen extraction fraction, CBF: cerebral blood flow, $CMRO_2$: cerebral metabolic rate of oxygen.

Region	Feature	Accuracy	Sensitivity	Specificity	AUC (range)
CET	OEF	81%	87%	75%	0.79 (0.76-0.84)
	CBF	71%	70%	71%	0.67 (0.55-0.73)
	$CMRO_2$	63%	27%	95%	0.52 (0.41-0.68)
NET2	OEF	68%	70%	66%	0.65 (0.46-0.82)
	CBF	73%	54%	89%	0.69 (0.64-0.75)
	$CMRO_2$	73%	44%	99%	0.66 (0.61-0.71)
CET/NET2	OEF	69%	60%	78%	0.66 (0.55-0.77)
	CBF	75%	63%	86%	0.80 (0.77-0.82)
	$CMRO_2$	83%	85%	82%	0.85 (0.73-0.93)
Best combined	OEF_{CET} + $CMRO_{2\,CET/NET2}$	93%	99%	88%	0.94 (0.88-0.96)

RESULTS

The scatterplot depicted in Figure 17 shows the predicted class values from the linear kernel SVM model, trained with two features: OEF in CET and the ratio of $CMRO_2$ in CET divided by NET2. 14 out of 15 tumors were correctly classified, with one cerebral metastasis being incorrectly classified as a glioblastoma (blue x). The incorrectly classified metastasis showed the lowest OEF in CET among the metastases and the second lowest OEF in CET across all patients included in this study, leading to a higher likelihood of an erroneous classification as a glioblastoma.
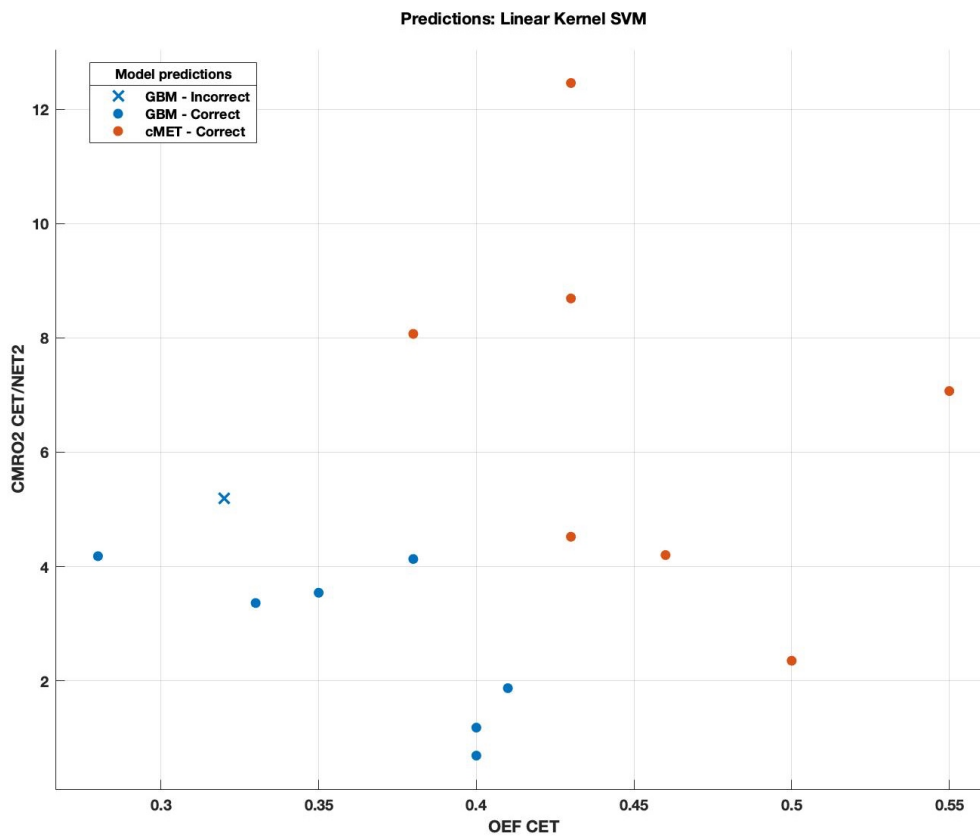
Figure 17: Scatterplot for class values as predicted by the trained linear kernel SVM, showing OEF in contrast-enhancing tumor (OEF CET) on the x-axis and the ratio CMRO2 CET/NET2 on the y-axis. Blue dots are correctly classified glioblastomas (GBM), orange dots are correctly classified cerebral metastases (cMET) and the blue cross is an incorrectly classified cerebral metastasis, erroneously predicted as a glioblastoma.

In Figure 18, a parallel coordinates plot depicts the predicted class values from the linear kernel SVM model, trained with two features: OEF in CET and the ratio of $CMRO_2$ in CET divided by NET2. Each of the features is represented on one of the vertical axes that show the standard deviation from the mean of the feature across all 15 patients examined in this study. There are two clusters visible with partly overlapping borders, the upper one being formed by the cerebral metastases and the lower one consisting of the glioblastomas. The incorrectly classified tumor is a metastasis that is more in line with the glioblastomas in terms of OEF in CET and is at the lower spectrum of the $CMRO_2$ $_{CET/NET2}$ ratio in the metastasis group.
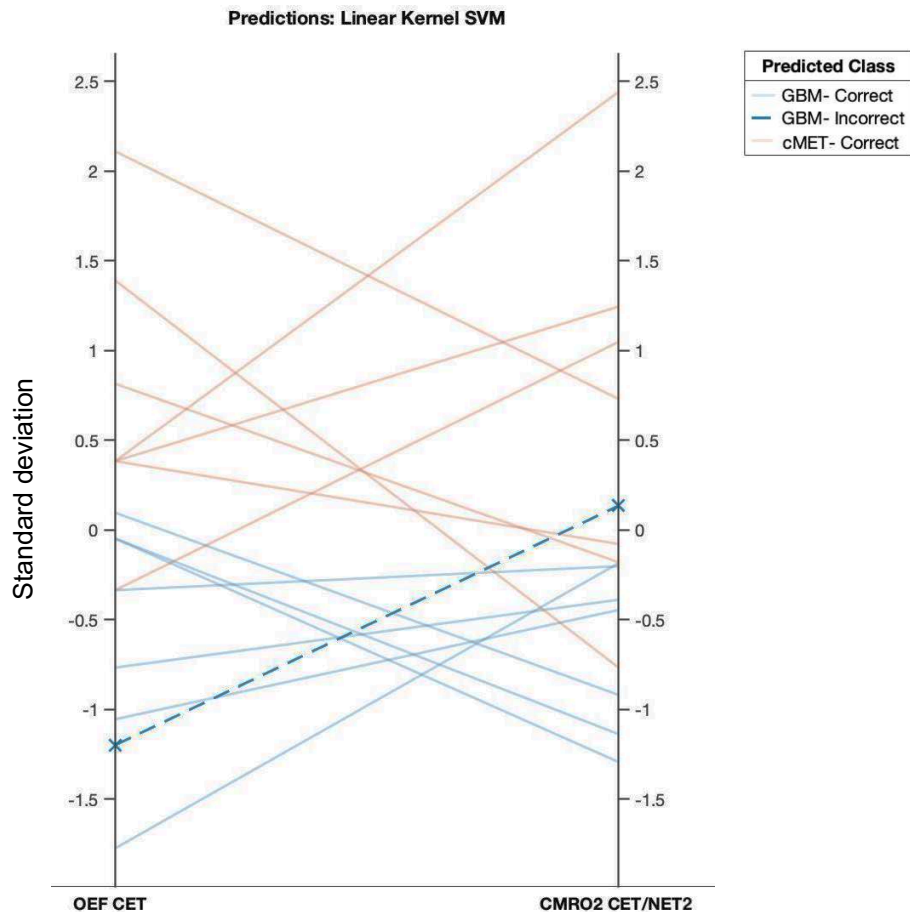
Figure 18: Parallel coordinates plot for class values as predicted by the trained linear kernel SVM, showing deviation from the mean for each observation. The left axis shows the standard deviation from mean OEF in contrast-enhancing tumor (OEF CET) across all 15 patients. The right axis shows the standard deviation from the mean of the ratio $CMRO_2$ $_{CET/NET2}$ across all 15 patients. Blue solid lines are correctly classified glioblastomas (GBM), orange solid lines are correctly classified cerebral metastases (cMET) and the blue dotted line is an incorrectly classified cerebral metastasis, predicted as a glioblastoma. NET2: non-enhancing T2 FLAIR hyperintense peritumoral ROI.

4 DISCUSSION

4.1 Discussion of oxygenation and perfusion results

In this study, the MRI-based QSM + qBOLD approach for OEF and $CMRO_2$ estimation was applied for the first time to a prospectively recruited collective of glioblastoma and cerebral metastasis patients in order to distinguish the two entities based on their respective cerebral oxygenation and perfusion characteristics. All results are systematically discussed and compared to previous research findings in literature. The order of subsections largely follows that of the results chapter.

4.1.1 Oxygenation and perfusion maps

The OEF and $CBF/CMRO_2$ maps displayed in Figure 6 and Figure 7 give a visual representation of the oxygenation parameters that were estimated for the entire brain of a 71-year-old male glioblastoma patient, exemplifying the differences between tumor and surrounding tissue that were present in the other patients, too. With regards to OEF maps, cerebral sulci and gyri with cerebrospinal fluid can be much better discriminated on the ANN map and are at times not even visible at all on the clustering-generated map. The X-means clustering map shows a generally lower level of OEF across the whole brain than the one calculated using the ANN. Particularly in the central part of the CET region, OEF is only slightly higher than in the surrounding tissue on the clustering image, while the ANN map shows substantially higher central OEF values with distinctly lower OEF in NET2, also compared to the surrounding, normal-appearing brain tissue. The higher contrast between tumor and surrounding tissue achieved by the ANN is one of the reasons why the OEF values it produced were used for binary classification with a support-vector machine in this study.

The aforementioned central OEF "hyperintensity" found within the glioblastoma CET region can be explained by examining the heterogenous tumor microenvironment and the different compartments of the tumor. OEF was found to be significantly lower across the vital parts of glioblastoma than in cNAB tissue and in the metastasis CET ROI, with the central necrotic areas excluded from this calculation (cf. tumor and necrosis ROIs in section 2.3 Image processing). In these central necrotic areas, which result from the tumor outgrowing its blood and nutrient supply (Pope, 2018), OEF is elevated beyond 75% due to "a high percentage of defective tumor vasculature", leading to inefficient perfusion (Stadlbauer et al., 2020). The finding of vital glioblastoma tissue showing lower values for OEF than cNAB tissue echoes previous results from an ANN-based feasibility study for MRI-derived OEF performed on a single glioblastoma patient: a distinct OEF "hotspot" was found within the tumor area with lower OEF in surrounding tissue (Domsch et al., 2018). This may be due to an "abnormally increased perfusion" in vital parts of the tumor (Stadlbauer et al., 2017b).

DISCUSSION

4.1.2 Results in CET, cNAB and NET2

In the CET regions of glioblastoma and cerebral metastasis patients, the only difference between the two groups that was found to be significant was in OEF (36 ± 5% versus 44 ± 7% in glioblastoma and metastases, respectively). This parameter may therefore be useful in distinguishing the two entities based on MR imaging. The high standard deviation for CBF and $CMRO_2$ is largely explained by two outliers with much higher perfusion values: One is the first glioblastoma patient whose perfusion was measured with a 3D pCASL sequence using a 32-channel head coil. This measurement yielded outsized CBF values throughout the entire brain leading to a positive outlier in CET and cNAB. The other is a metastasis patient with very high tumor perfusion and normal CBF in the remainder of the brain; hence, there is only a positive outlier in the CET region and not in cNAB.

None of the differences between CET and NET2 in glioblastoma patients were significant, whereas all mean values for OEF, CBF and $CMRO_2$ across metastasis patients were significantly higher in the CET region than in the surrounding NET2 region. These results largely reflect the findings of two earlier MRI-based studies that looked at 21 glioblastoma and 12 high-grade glioma (11 glioblastomas, one WHO grade III glioma) patients (Stadlbauer et al., 2017b; Preibisch et al., 2017). They determined OEF in CET to be 35 ± 17% and 25 ± 8%, respectively. The former study very closely matches the ANN results of this study while the latter is more in line with OEF from X-means clustering. The same studies found oxygen extraction to be higher in cNAB tissue than in CET with OEF values of 72 ± 7% and 49 ± 4%. Similarly, this study found OEF values in cNAB of glioblastoma patients to be significantly higher than in CET.

One of these studies also published values for CBF: perfusion was relatively high in CET and much lower in "healthy" brain (Preibisch et al., 2017). That is comparable to the findings of this study, with CBF values in CET significantly higher than in cNAB tissue. The absolute CBF value in cNAB of glioblastoma patients (40 ± 27ml/100g/min) is right between the values found in said MR study (Preibisch et al., 2017) and a ^{15}O-PET study that did, however, not systematically exclude any kind of brain tumor (Lammertsma et al., 1983), indicating that the CBF values obtained from arterial spin labeling are rather robust. This is further supported by two studies that list physiological ranges for brain perfusion obtained using ASL sequences: While in grey matter, CBF is expected to be between 40 and 70ml/100g/min according to one source (Deibler et al., 2008) and between 60 to 110ml/100g/min according to another (van Gelderen et al., 2008), white matter CBF has been reported to be between 10 and 80ml/100g/min (van Gelderen et al., 2008).

$CMRO_2$ was found in one study to be 194 ± 62µmol/100g/min in CET (Stadlbauer et al., 2017b), which is close to this study's findings in glioblastoma and can be interpreted as being well within the margin of interindividual differences in perfusion. At 132 ± 16µmol/100g/min, the same research group found an identical $CMRO_2$ in cNAB as this study. Both MRI studies on glioblastoma patients mentioned above found reduced OEF and increased CBF in glioblastoma CET when compared with cNAB or "healthy" brain tissue, with a positive net effect on $CMRO_2$ because of the disproportionally higher perfusion in tumor tissue (Stadlbauer et al., 2017b; Preibisch et al., 2017). This effect was also found in this study, leading to comparable results for the glioblastoma group.

The QSM + qBOLD approach for estimation of OEF employed in this study (with the X-means algorithm described in section 2.5.2) was put to the test in 2019 on eight high-grade glioma patients (six glioblastomas and two anaplastic astrocytomas), using dynamic contrast-enhanced data for CBF reconstruction instead of arterial spin labeling (Hubertus et al., 2019c). In accordance with the results of this study, their findings showed significantly reduced OEF

and significantly increased CBF in glioblastoma tissue. This inverse relationship is further supported by the results of a previous study which concluded that high-grade gliomas generally exhibit lower OEF values in the CET region, indicating a high vascular oxygenation that is accompanied by the high CBF values typically observed in well-perfused tissue (Preibisch, 2017).

Both the glioblastoma and the metastasis group showed just that: higher CBF paired with lower OEF in CET compared to the cNAB regions in the patients' brains. A possible explanation is a higher vascularization due to angiogenic factors produced by the tumor, one of the hallmarks of cancer (Hanahan and Weinberg, 2000; 2011), and less efficient oxygen extraction due to a physiologically inferior capillary configuration (Stadlbauer et al., 2017b).

Two studies found OEF to be clearly higher in the peritumoral edema than in CET (Stadlbauer et al., 2017b; Preibisch et al., 2017). It is argued in one of these studies that in edema, the combined effect of low perfusion due to high interstitial pressure and initial proliferation might elicit mildly hypoxic conditions similar to hypoxemia (Preibisch et al., 2017). Possibly owing to the described high interstitial pressure in peritumoral edema, the two glioblastoma studies found much lower CBF and $CMRO_2$ values in NET2, supporting the results of this study. The OEF values they estimated for the peritumoral region stand in contrast to this study's findings, though. Here, OEF was lower in NET2 than in CET, confirming the results of a different study that observed very low OEF values in peritumoral edema (Hubertus et al., 2019c). This was interpreted as an indication that the tissue, having been infiltrated by glioma cells, might not be viable anymore. Another study correlated histopathological findings of infiltrative growth in the peritumoral region of glioblastoma with higher perfusion (Sunwoo et al., 2016). Ceteris paribus, higher perfusion should lead to lower oxygen extraction; this effect has already been described for the CET region (Stadlbauer et al., 2017b). A PET/MR study with a sufficiently large number of patients might be needed to shed light on true OEF in the peritumoral region surrounding the contrast-enhancing part of glioblastomas.

With regards to oxygenation and perfusion in and around cerebral metastases, little research has been publicized, perhaps because of the heterogeneity of the group that originates from the many different possible primary cancers influencing metastasis physiology. Three studies that examined the differences in normalized and relative cerebral blood flow (nCBF and rCBF) and rCBV between glioblastomas and brain metastases came to similar conclusions as this study, finding higher perfusion values in CET as well as the peritumoral edema regions of glioblastomas when compared to the corresponding regions in metastasis patients (Sunwoo et al., 2016; Server et al., 2011; Bauer et al., 2015). These studies unanimously found a reduced ratio of perfusion or blood volume (relative/normalized $CBF_{CET/NET2}$ or $rCBV_{CET/NET2}$) in CET divided by NET2 in glioblastomas compared to brain metastases, a difference that this study reproduced.

Additionally, this study compared the ratio of $CMRO_2$ in CET divided by NET2 which yielded a highly significant difference between the two tumor groups, making $CBF_{CET/NET2}$ and $CMRO_2$ $_{CET/NET2}$ likely candidates to allow for a differentiation between the two tumor groups. These results are in accordance with the hypothesized differences in perfusion and oxygenation in and around glioblastomas and cerebral metastases and support the notion that the infiltrative growth pattern of high-grade gliomas increases their peritumoral oxygen metabolism and makes them distinguishable from rather circumscribed metastatic brain tumors.

DISCUSSION

4.1.3 Comparison of ANN and clustering results

In order to inform a decision about which features to choose for the ROC analysis, ANN or clustering-derived OEF and $CMRO_2$, the values obtained from both approaches were compared using Bland-Altman diagrams and significance analyses. In glioblastoma and metastasis patients alike, ANN produced higher values than clustering for both parameters, with the difference in OEF being statistically significant.

When contrasting global OEF in healthy individuals from earlier studies with OEF found in this study in cNAB tissue, assumed to be healthy and normal in perfusion and oxygenation, it becomes apparent that ANN should be preferred when evaluating OEF in healthy brain tissue. Healthy global brain OEF at rest was consistently found to be about 40% in previous research, with MR BOLD-based studies estimating it at $41.6 \pm 1.8\%$ (An and Lin, 2000), $38.3 \pm 5.3\%$ (He and Yablonskiy, 2007) and $40 \pm 1\%$ (Domsch et al., 2018). A Japanese multicenter study that used ^{15}O as tracer in a total of 70 healthy individuals for a PET study found a mean whole-brain OEF of $44 \pm 6\%$ (Ito et al., 2004). Another PET study described OEF at rest to be uniform and homogenous across the whole brain due to the brain's autoregulation (Gusnard and Raichle, 2001). A landmark ^{15}O-PET study conducted in 1983 determined the regional oxygen extraction ratio rOER (which is analogous to OEF) in the contralateral (assumed to be healthy) grey matter of tumor patients to be $47 \pm 8\%$ with a significantly lower rOER in tumor tissue (Lammertsma et al., 1983). However, there was no breakdown given about the entities included in the tumor group, so these results should be taken with caution when transferring them to the glioblastoma and cerebral metastasis subset of patients looked at in this study. A later research project featuring ^{15}O-PET imaging looked at the OEF of glioma patients before and after radiotherapy: mean OEF in contralateral grey matter of four glioblastoma patients was found to be $53.7 \pm 10.7\%$ pre-radiation (Ogawa et al., 1998).

This should be seen in conjunction with the OEF data from two studies that looked at regions of interest analogous to those examined in this study, namely CET, NET2 and cNAB, and are largely in line with the ANN results (Stadlbauer et al., 2017b; Preibisch et al., 2017). These values put the ANN method in a favorable light as the average OEF in cNAB across all patients of 45% and mean OEF in cNAB of glioblastoma patients of 43% reproduce the OEF of previous studies more closely than the values estimated using X-means clustering. Particularly in light of the higher OEF found in studies which made use of ^{15}O gas tracers (Ito et al., 2004; Lammertsma et al., 1983; Ogawa et al., 1988), which are widely considered as the reference standard in measuring OEF and $CMRO_2$ (Fan et al., 2020), it is very well possible that the X-means clustering approach used in this study substantially underestimates OEF and therefore $CMRO_2$.

In summary, ANN and clustering deliver significantly different values for OEF with the ANN being closer to the values found in previous studies. This leads the author to assume that the ANN may yield a more robust estimate which is more likely to make the differentiation of glioblastoma and cerebral metastasis possible. The accordance of the ANN-derived results with earlier research in combination with its (physiologically accurate) lack of OEF signal in cerebrospinal fluid, outlined in detail in section 4.1.1, lead to the features from the ANN method being preferred for predicting the tumor class in the following section.

DISCUSSION

4.1.4   ROC analysis with a linear kernel SVM classifier

The receiver operating curve analysis performed in this study showed a maximum accuracy of 93% (99% sensitivity, 88% specificity) with an AUC of 0.94 in the binary classification of glioblastoma and cerebral metastasis. The features used for training a multivariable linear kernel support-vector machine for this classification problem were OEF in CET and the ratio $CMRO_{2\ CET/NET2}$. Adding OEF improved the classification performance compared to a $CMRO_{2\ CET/NET2}$-only classifier (accuracy: 83%, AUC: 0.85) despite it being part of the $CMRO_2$ equation. An SVM was chosen for classification since it emerged as the best classifier delivering the highest accuracy in a number of studies that compared it to different approaches such as Naïve Bayes, KNN and decision trees for binary classification of glioblastoma/cerebral metastasis (Shrot et al., 2019; Artzi et al., 2019; Tsolaki et al., 2013). To confirm this, a 5-fold cross-validated multivariable training run across a number of different classifier algorithms including KNN, decision trees, logistic regression, Naïve Bayes, linear kernel SVM, quadratic kernel SVM and Gaussian SVM was performed in the MATLAB R2020b Classification Learner toolbox, using the two features OEF_{CET} and $CMRO_{2\ CET/NET2}$. The linear kernel SVM classifier emerged as the one with the highest accuracy, with the KNN classifier presenting another good classification algorithm, achieving similar accuracy but a slightly lower AUC.

In a meta-analysis of 18 MR perfusion-based studies that aimed at differentiating glioblastoma from brain metastasis, the pooled sensitivity and specificity was 90% and 91%, respectively, with a hierarchical summary ROC area under the curve of 0.96 (Suh et al., 2018). A study that compared rCBF ratios of CET/NET2 between glioblastoma and cerebral metastasis yielded an AUC of 0.92 (Server et al., 2011). These classifier performances put the diagnostic performance shown in this study well in the vicinity of previous classifiers based on perfusion MRI.

Additionally, the classification accuracy achieved in this study should not be underestimated when comparing it to the current standard of practice: invasive stereotactic biopsies. To the best of the author's knowledge, no study has previously analyzed the accuracy of stereotactic biopsy in the discrimination of glioblastoma and cerebral metastasis. However, systematic accuracy rates have been determined for frameless and frame based stereotactic neurosurgical tumor biopsies. Their diagnostic yield lies between 90 and 100% (Sciortino et al., 2019; Chernov et al., 2009), with histological diagnoses still representing a potential obstacle in correctly diagnosing the lesion in question. Two studies estimated the diagnostic accuracy, i.e. the agreement of histological diagnosis after biopsy and after surgical resection, at between 79 and 89% (Chernov et al., 2009; Woodworth et al., 2005), with frameless systems usually performing better (Woodworth et al., 2005). Therefore, while a stereotactic biopsy may be the only clinically available option at the moment that makes histological grading possible and enables the analysis of IDH and O-6-methylguanine-DNA methyltransferase (MGMT) methylation status for glioblastoma (Sciortino et al., 2019), it still is a (minimally) invasive procedure with risk of brain injury, possibly resulting in transient or even permanent neurological deficit (Gralla et al., 2003). In light of the imperfect accuracy rate of biopsies, MR-based diagnostic tools such as the one used in this study with accuracy rates beyond 90% may present a way forward for noninvasive, reliable tumor differentiation – and grading (Stadlbauer et al., 2017b) – in order to inform therapeutic decisions.

In addition to the similar diagnostic performance that this study achieved compared to previous research, the underlying parameters yield quite useful information about tumor metabolism and aggressiveness. $CMRO_2$ in tumor has been found to be a predictor for antiangiogenic response of glioblastoma to the humanized monoclonal antibody to VEGF-A, bevacizumab (Bonekamp et al., 2017). Not only does it allow to predict tumor vascular response, $CMRO_2$ at

baseline, i.e. before therapy, has also been shown to be a predictor of progression-free survival (PFS) (Kickingereder et al., 2020). Another benefit of this imaging method may be the possibility of pre-selecting glioblastoma patients for treatment with radiotherapy (Preibisch et al., 2017) or antiangiogenic therapy based on oxygen metabolism, which has been linked to favorable overall survival when applied to patients with low baseline $CMRO_2$ in tumor (Kickingereder et al., 2020). It can further be used to monitor treatment response after initial therapy in terms of changes to $CMRO_2$ with the possibility to use it for resection control and detection of residual tumor (Stadlbauer et al., 2017a).

4.2 Limitations

The QSM + qBOLD approach employed for OEF estimation in this study is subject to a number of limitations. Although the results appear to be plausible when compared to literature values, QSM + qBOLD requires a set of assumptions about physiologic parameters that were not measured for each individual patient. Among these assumptions are a constant tissue hematocrit and a constant arterial oxygen saturation. In vivo, these parameters might differ considerably between patients. Further, the OEF values from QSM + qBOLD are prone to susceptibility artifacts from iron accumulations in deep grey matter or from blood degradation metabolites from hemorrhage, a phenomenon not uncommon in the necrotic center of glioblastomas and cerebral metastases. Susceptibility is also vulnerable to disturbances close to air-tissue bounds, e.g. the sinus frontalis.

Further, the patient population included in this study was rather small but was quite homogenous, consisting of two well-defined, almost identically-sized groups in a relatively narrow age range. However, the brain metastases originating from different primary tumors may cause different oxygen metabolism characteristics between them, a possibility that is not reflected in this study as there was no special analysis performed on brain metastases broken down by primary tumor. The same applies to glioblastoma patients that were not stratified according to IDH or MGMT promoter methylation status. It is therefore recommended to test the results of this study with a larger patient population so that informed statements about tumor subgroups can be derived.

Lastly, the different regions of interest in this study were traced by hand, the results are subject to intra- and inter-observer variability. This was mitigated by the fact that oxygenation and perfusion parameters were averaged across voxels contained within the ROIs, making them less susceptible to small differences in manual outlining and segmentation. Tumor ROIs were mirrored at the midline to generate ROIs for contralateral normal-appearing brain, leading to the latter consisting of a variable mix of grey and white matter. This may have had an impact on the estimation of perfusion and oxygenation parameters.

4.3 Suggestions for future research

The ability to non-invasively image OEF and $CMRO_2$ has tremendous clinical value. $CMRO_2$ allows for estimating the metabolic activity of tumors, following the underlying principle that highly proliferative, malignant tumors produce angiogenic growth factors, increasing their vascularization to satisfy their metabolic needs. In such a highly dynamic microenvironment, especially within very aggressive tumors such as glioblastoma, the metabolic rate of oxygen may be quite heterogenous. Therefore, a more granular look at how $CMRO_2$ varies within these tumors and in their surrounding tissue might yield an insight into the proliferative potential and metabolism of the malign tumor.

On the topic of $CMRO_2$ in perifocal edema, further research into oxygen metabolism gradients around the enhancing part of glioblastoma could also be of interest to determine tissue that has already been infiltrated by tumor cells. A histopathological study correlating infiltration with OEF, CBF and $CMRO_2$ in the peritumoral region might shed more light on this subject, possibly enabling surgeons to get a more complete picture of compromised brain tissue before resection.

Another promising area for further research that could utilize this study as a reference point is an assessment of how perfusion and oxygenation parameters change after an initial therapy of the evaluated tumors. This could help in understanding how tumor metabolism reacts to radiation and chemotherapy and may be useful as an early warning sign of relapse before the recurrent tumor becomes visible in contrast-enhanced imaging, signaling an already disrupted blood-brain barrier.

4.4 Conclusion

It was the objective of this study to apply for the first time the QSM + qBOLD approach for OEF and $CMRO_2$ estimation to a prospectively recruited collective of glioblastoma and brain metastasis patients in order to find differences in their cerebral oxygenation and perfusion. Based on the hypothesis that OEF, CBF and $CMRO_2$ would enable their discrimination due to the infiltrative growth pattern of glioblastomas and the lack thereof in metastases, a machine learning classifier was trained to reliably differentiate the two entities, analyzing the oxygenation and perfusion parameters in CET and proximal NET2.

The highest discriminative power was achieved when using two features: OEF in CET and the ratio of $CMRO_2$ in CET divided by NET2. This takes advantage of the pathophysiological differences in glioblastomas and brain metastases outlined above. With an accuracy of 93% and an AUC of 0.94, the two entities could be differentiated quite well with a linear kernel support-vector machine classifier. On top of the good predictive accuracy this method achieved, the $CMRO_2$ it yields is an important physiological parameter that can be used to predict tumor response to radiation and antiangiogenic therapy as well as progression-free survival in glioblastoma patients.

In conclusion, OEF and $CMRO_2$ derived from QSM + qBOLD appear to be robust and can be a valuable tool for differentiating glioblastoma from cerebral metastasis. The methods employed in this study have the potential to substantially improve prediction of therapy outcomes for glioblastoma. Therefore, they are promising candidates for implementation into the clinical routine, not least to complement and, in the long run, potentially replace current MRI sequences that require administration of intravenous contrast agent.

5 SUMMARY

Purpose: This prospective clinical study was aimed at differentiating glioblastoma and cerebral metastasis, two tumor entities that often show similar radiological features, by means of combined MR oxygenation and perfusion imaging. Their distinction is highly important due to vastly differing therapy algorithms as well as patient outcomes. It was hypothesized that the infiltrative growth pattern of glioblastomas and the lack thereof in brain metastases would make it possible to distinguish the two groups based on their metabolic parameters in and around the contrast-enhancing part of the tumor.

Materials and Methods: Fifteen previously untreated patients were recruited, seven of which suffered from glioblastoma (median age: 68 years, range: 54 – 84 years) with the remaining eight showing one or multiple brain metastases (median age 66 years, range: 50 – 78 years). All patients underwent preoperative MRI scans including multi-gradient echo and pseudo-continuous arterial spin labeling sequences. Three regions of interest were segmented in post-processing: contrast-enhancing tumor (CET), contralateral normal-appearing brain tissue (cNAB) and peritumoral non-enhancing T2-weighted fluid-attenuated inversion recovery hyperintense area (NET2). For these regions, oxygen extraction fraction (OEF) and cerebral blood flow (CBF) were estimated, yielding a third parameter: cerebral metabolic rate of oxygen ($CMRO_2$). Two different machine learning-based approaches were employed to calculate OEF: an artificial neural network (ANN) and X-means clustering, both estimating the solution of the quantitative susceptibility mapping and quantitative blood-oxygen-level-dependent model (QSM + qBOLD). ANN results were used for statistical analysis and as features for training a support-vector machine algorithm for binary classification of tumor type. Classification performance was determined with receiver operating characteristic (ROC) analysis.

Results: We demonstrated that OEF in CET was significantly lower ($p = 0.03$) in glioblastomas than metastases, all features (OEF, CBF and $CMRO_2$) were significantly higher ($p = 0.01$) in CET than NET2 for metastasis patients only, and the ratios of CET/NET2 for CBF ($p = 0.04$) and $CMRO_2$ ($p = 0.01$) were significantly higher for metastasis patients than for glioblastoma patients. For glioblastoma patients, OEF was shown to be significantly lower ($p = 0.02$) in CET than in cNAB. In ROC analysis, the ratios of $CMRO_2$ and CBF in CET divided by NET2 were found to be the best single characteristics for classification with areas under the curve of 0.85 and 0.80, respectively. The best multiparametric classification model was found when training the classifier on two features: OEF in CET and the $CMRO_2$ ratio of CET/NET2. The resulting model had an area under the ROC curve of 0.94 with 93% classification accuracy.

Conclusion: The differences in oxygenation and perfusion between glioblastomas and brain metastases support the research hypothesis and allow for robust, non-invasive differential diagnosis of the tumor entity. While classification performance was found to be in line with previous MR-based publications that mainly investigated perfusion metrics such as cerebral blood flow and volume, the voxelwise estimation of $CMRO_2$ presents a major advantage in that it may also yield an insight into the likely response to radiation, antiangiogenic and chemotherapy, especially in glioblastoma. This makes the methods employed in this study promising candidates for implementation into the clinical routine, not least to complement anatomical MRI sequences without the need for additional application of contrast agent. In the long run, they have the potential to add to or even replace brain biopsies due to the good classification accuracy and the absence of typical complications of an invasive procedure. However, further research with larger patient populations is required before the QSM + qBOLD model can find its way into clinical decision making.

6 LITERATURE

Abdel Razek, A.A.K., Talaat, M., El-Serougy, L., Abdelsalam, M., and Gaballa, G. (2019). Differentiating Glioblastomas from Solitary Brain Metastases Using Arterial Spin Labeling Perfusion- and Diffusion Tensor Imaging-Derived Metrics. World Neurosurg 127, e593-e598.

Alsop, D.C., Detre, J.A., Golay, X., Gunther, M., Hendrikse, J., Hernandez-Garcia, L., Lu, H., MacIntosh, B.J., Parkes, L.M., Smits, M.*, et al.* (2015). Recommended implementation of arterial spin-labeled perfusion MRI for clinical applications: A consensus of the ISMRM perfusion study group and the European consortium for ASL in dementia. Magn Reson Med *73*, 102-116.

American Association of Neurological Surgeons (2021). Brain Tumors (https://www.aans.org/en/Patients/Neurosurgical-Conditions-and-Treatments/Brain-Tumors). Accessed: January 18, 2021.

An, H., and Lin, W. (2000). Quantitative measurements of cerebral blood oxygen saturation using magnetic resonance imaging. J Cereb Blood Flow Metab 20, 1225-1236.

Artzi, M., Bressler, I., and Ben Bashat, D. (2019). Differentiation between glioblastoma, brain metastasis and subtypes using radiomics analysis. J Magn Reson Imaging 50, 519-528.

Askaner, K., Rydelius, A., Engelholm, S., Knutsson, L., Latt, J., Abul-Kasim, K., and Sundgren, P.C. (2019). Differentiation between glioblastomas and brain metastases and regarding their primary site of malignancy using dynamic susceptibility contrast MRI at 3T. J Neuroradiol 46, 367-372.

Bauer, A.H., Erly, W., Moser, F.G., Maya, M., and Nael, K. (2015). Differentiation of solitary brain metastasis from glioblastoma multiforme: a predictive multiparametric approach using combined MR diffusion and perfusion. Neuroradiology 57, 697-703.

Blasel, S., Jurcoane, A., Franz, K., Morawe, G., Pellikan, S., and Hattingen, E. (2010). Elevated peritumoural rCBV values as a mean to differentiate metastases from high-grade gliomas. Acta Neurochir (Wien) 152, 1893-1899.

Bonekamp, D., Mouridsen, K., Radbruch, A., Kurz, F.T., Eidel, O., Wick, A., Schlemmer, H.P., Wick, W., Bendszus, M., Ostergaard, L.*, et al.* (2017). Assessment of tumor oxygenation and its impact on treatment response in bevacizumab-treated recurrent glioblastoma. J Cereb Blood Flow Metab *37*, 485-494.

Chernov, M.F., Muragaki, Y., Ochiai, T., Taira, T., Ono, Y., Usukura, M., Maruyama, T., Nakaya, K., Nakamura, R., Iseki, H., et al. (2009). Spectroscopy-supported frame-based image-guided stereotactic biopsy of parenchymal brain lesions: comparative evaluation of diagnostic yield and diagnostic accuracy. Clin Neurol Neurosurg 111, 527-535.

Cho, J., Kee, Y., Spincemaille, P., Nguyen, T.D., Zhang, J., Gupta, A., Zhang, S., and Wang, Y. (2018). Cerebral metabolic rate of oxygen (CMRO2) mapping by combining quantitative susceptibility mapping (QSM) and quantitative blood oxygenation level-dependent imaging (qBOLD). Magn Reson Med *80*, 1595-1604.

Cho, J., Zhang, S., Kee, Y., Spincemaille, P., Nguyen, T.D., Hubertus, S., Gupta, A., and Wang, Y. (2020). Cluster analysis of time evolution (CAT) for quantitative susceptibility mapping (QSM) and quantitative blood oxygen level-dependent magnitude (qBOLD)-based oxygen extraction fraction (OEF) and cerebral metabolic rate of oxygen (CMRO2) mapping. Magn Reson Med *83*, 844-857.

Cortes, C., Vapnik, V. (1995). Support-Vector Networks. Machine Learning 20, 273-297.

de Rochefort, L., Liu, T., Kressler, B., Liu, J., Spincemaille, P., Lebon, V., Wu, J., and Wang, Y. (2010). Quantitative susceptibility map reconstruction from MR phase data using bayesian regularization: validation and application to brain imaging. Magn Reson Med *63*, 194-206.

Deibler, A.R., Pollock, J.M., Kraft, R.A., Tan, H., Burdette, J.H., and Maldjian, J.A. (2008). Arterial spin-labeling in routine clinical practice, part 3: hyperperfusion patterns. AJNR Am J Neuroradiol 29, 1428-1435.

Domsch, S., Murle, B., Weingartner, S., Zapp, J., Wenz, F., and Schad, L.R. (2018). Oxygen extraction fraction mapping at 3 Tesla using an artificial neural network: A feasibility study. Magn Reson Med *79*, 890-899.

Dong, F., Li, Q., Jiang, B., Zhu, X., Zeng, Q., Huang, P., Chen, S., and Zhang, M. (2020). Differentiation of supratentorial single brain metastasis and glioblastoma by using peri-enhancing oedema region-derived radiomic features and multiple classifiers. Eur Radiol 30, 3015-3022.

Fan, A.P., An, H., Moradi, F., Rosenberg, J., Ishii, Y., Nariai, T., Okazawa, H., and Zaharchuk, G. (2020). Quantification of brain oxygen extraction and metabolism with [(15)O]-gas PET: A technical review in the era of PET/MRI. Neuroimage 220, 117136.

Fink, K.R., and Fink, J.R. (2013). Imaging of brain metastases. Surg Neurol Int 4, S209-219.

Gavrilovic, I.T., and Posner, J.B. (2005). Brain metastases: epidemiology and pathophysiology. J Neurooncol 75, 5-14.

Giordana MT, Cordera S and Boghi A. Cerebral metastases as first symptom of cancer: a clinico-pathologic study. J Neurooncol 2000; 50: 265-273. 2001/03/27. DOI: 10.1023/a:1006413001375.

Gralla, J., Nimsky, C., Buchfelder, M., Fahlbusch, R., and Ganslandt, O. (2003). Frameless stereotactic brain biopsy procedures using the Stealth Station: indications, accuracy and results. Zentralbl Neurochir 64, 166-170.

Gusnard, D.A., Raichle, M.E., and Raichle, M.E. (2001). Searching for a baseline: functional imaging and the resting human brain. Nat Rev Neurosci 2, 685-694.

Hanahan, D., and Weinberg, R.A. (2000). The hallmarks of cancer. Cell 100, 57-70.

Hanahan, D., and Weinberg, R.A. (2011). Hallmarks of cancer: the next generation. Cell 144, 646-674.

Hardee, M.E., and Zagzag, D. (2012). Mechanisms of glioma-associated neovascularization. Am J Pathol 181, 1126-1141.

He, X., and Yablonskiy, D.A. (2007). Quantitative BOLD: mapping of human cerebral deoxygenated blood volume and oxygen extraction fraction: default state. Magn Reson Med *57*, 115-126.

Hubertus, S. (2019). Quantitative susceptibility mapping to measure the local tissue oxygenation. Dissertation. Combined Faculties for the Natural Sciences and for Mathematics, Heidelberg University.

Hubertus, S., Thomas, S., Cho, J., Zhang, S., Wang, Y., and Schad, L.R. (2019a). Using an artificial neural network for fast mapping of the oxygen extraction fraction with combined QSM and quantitative BOLD. Magn Reson Med *82*, 2199-2211.

Hubertus, S., Thomas, S., Cho, J., Zhang, S., Wang, Y., and Schad, L.R. (2019b). Comparison of gradient echo and gradient echo sampling of spin echo sequence for the quantification of the oxygen extraction fraction from a combined quantitative susceptibility mapping and quantitative BOLD (QSM+qBOLD) approach. Magn Reson Med *82*, 1491-1503.

Hubertus, S., Thomas, S., Cho, J., Zhang, S., Kovanlikaya, I., Wang, Y., Schad, L. R. (2019c). MRI-based oxygen extraction fraction and cerebral metabolic rate of oxygen mapping in high-grade glioma using a combined quantitative susceptibility mapping and quantitative blood oxygenation level-dependent approach. Paper presented at: Proceedings of the International Society for Magnetic Resonance in Medicine (Montréal, Canada).

LITERATURE

Ito, H., Kanno, I., Kato, C., Sasaki, T., Ishii, K., Ouchi, Y., Iida, A., Okazawa, H., Hayashida, K., Tsuyuguchi, N., et al. (2004). Database of normal human cerebral blood flow, cerebral blood volume, cerebral oxygen extraction fraction and cerebral metabolic rate of oxygen measured by positron emission tomography with 15O-labelled carbon dioxide or water, carbon monoxide and oxygen: a multicentre study in Japan. Eur J Nucl Med Mol Imaging 31, 635-643.

Kickingereder, P., Brugnara, G., Hansen, M.B., Nowosielski, M., Pfluger, I., Schell, M., Isensee, F., Foltyn, M., Neuberger, U., Kessler, T., et al. (2020). Noninvasive Characterization of Tumor Angiogenesis and Oxygenation in Bevacizumab-treated Recurrent Glioblastoma by Using Dynamic Susceptibility MRI: Secondary Analysis of the European Organization for Research and Treatment of Cancer 26101 Trial. Radiology 297, 164-175.

Lammertsma, A.A., Wise, R.J., Heather, J.D., Gibbs, J.M., Leenders, K.L., Frackowiak, R.S., Rhodes, C.G., and Jones, T. (1983). Correction for the presence of intravascular oxygen-15 in the steady-state technique for measuring regional oxygen extraction ratio in the brain: 2. Results in normal subjects and brain tumour and stroke patients. J Cereb Blood Flow Metab 3, 425-431.

Lee, E.J., Ahn, K.J., Lee, E.K., Lee, Y.S., and Kim, D.B. (2013). Potential role of advanced MRI techniques for the peritumoural region in differentiating glioblastoma multiforme and solitary metastatic lesions. Clin Radiol 68, e689-697.

Lee, E.J., terBrugge, K., Mikulis, D., Choi, D.S., Bae, J.M., Lee, S.K., and Moon, S.Y. (2011). Diagnostic value of peritumoral minimum apparent diffusion coefficient for differentiation of glioblastoma multiforme from solitary metastatic lesions. AJR Am J Roentgenol 196, 71-76.

Lehmann, P., Saliou, G., de Marco, G., Monet, P., Souraya, S.E., Bruniau, A., Vallee, J.N., and Ducreux, D. (2012). Cerebral peritumoral oedema study: does a single dynamic MR sequence assessing perfusion and permeability can help to differentiate glioblastoma from metastasis? Eur J Radiol 81, 522-527.

Lemercier, P., Paz Maya, S., Patrie, J.T., Flors, L., and Leiva-Salinas, C. (2014). Gradient of apparent diffusion coefficient values in peritumoral edema helps in differentiation of glioblastoma from solitary metastatic lesions. AJR Am J Roentgenol 203, 163-169.

Li, X., Wang, D., Liao, S., Guo, L., Xiao, X., Liu, X., Xu, Y., Hua, J., Pillai, J.J., and Wu, Y. (2020). Discrimination between Glioblastoma and Solitary Brain Metastasis: Comparison of Inflow-Based Vascular-Space-Occupancy and Dynamic Susceptibility Contrast MR Imaging. AJNR Am J Neuroradiol 41, 583-590.

Lin, L., Xue, Y., Duan, Q., Sun, B., Lin, H., Huang, X., and Chen, X. (2016). The role of cerebral blood flow gradient in peritumoral edema for differentiation of glioblastomas from solitary metastatic lesions. Oncotarget 7, 69051-69059.

Ma, Y., Mazerolle, E.L., Cho, J., Sun, H., Wang, Y., and Pike, G.B. (2020). Quantification of brain oxygen extraction fraction using QSM and a hyperoxic challenge. Magn Reson Med 84, 3271-3285.

Malone H, Yang J, Hershman DL, et al. Complications Following Stereotactic Needle Biopsy of Intracranial Tumors. World Neurosurg 2015; 84: 1084-1089. 2015/05/27. DOI: 10.1016/j.wneu.2015.05.025.

Nayak, L., Lee, E.Q., and Wen, P.Y. (2012). Epidemiology of brain metastases. Curr Oncol Rep 14, 48-54.

Noroxe, D.S., Poulsen, H.S., and Lassen, U. (2016). Hallmarks of glioblastoma: a systematic review. ESMO Open *1*, e000144.

Ogawa, T., Uemura, K., Shishido, F., Yamaguchi, T., Murakami, M., Inugami, A., Kanno, I., Sasaki, H., Kato, T., Hirata, K., et al. (1988). Changes of cerebral blood flow, and oxygen and glucose metabolism following radiochemotherapy of gliomas: a PET study. J Comput Assist Tomogr 12, 290-297.

Ostrom, Q.T., Wright, C.H., and Barnholtz-Sloan, J.S. (2018). Brain metastases: epidemiology. Handb Clin Neurol 149, 27-42.

Paech, D., Nagel, A.M., Schultheiss, M.N., Umathum, R., Regnery, S., Scherer, M., Wick, A., Platt, T., Wick, W., Bendszus, M., et al. (2020). Quantitative Dynamic Oxygen 17 MRI at 7.0 T for the Cerebral Oxygen Metabolism in Glioma. Radiology 295, 181-189.

Pelleg, D., Moore, A. (2000). X-means: Extending K-means with Efficient Estimation of the Number of Clusters Paper presented at: Proceedings of the Seventeenth International Conference on Machine Learning (San Francisco, California, USA).

Pope, W.B. (2018). Brain metastases: neuroimaging. Handb Clin Neurol 149, 89-112.

Preibisch, C., Shi, K., Kluge, A., Lukas, M., Wiestler, B., Gottler, J., Gempt, J., Ringel, F., Al Jaberi, M., Schlegel, J., et al. (2017). Characterizing hypoxia in human glioma: A simultaneous multimodal MRI and PET study. NMR Biomed *30*.

Sciortino, T., Fernandes, B., Conti Nibali, M., Gay, L.G., Rossi, M., Lopci, E., Colombo, A.E., Elefante, M.G., Pessina, F., Bello, L., et al. (2019). Frameless stereotactic biopsy for precision neurosurgery: diagnostic value, safety, and accuracy. Acta Neurochir (Wien) 161, 967-974.

Server, A., Orheim, T.E., Graff, B.A., Josefsen, R., Kumar, T., and Nakstad, P.H. (2011). Diagnostic examination performance by using microvascular leakage, cerebral blood volume, and blood flow derived from 3-T dynamic susceptibility-weighted contrast-enhanced perfusion MR imaging in the differentiation of glioblastoma multiforme and brain metastasis. Neuroradiology 53, 319-330.

Shrot, S., Salhov, M., Dvorski, N., Konen, E., Averbuch, A., and Hoffmann, C. (2019). Application of MR morphologic, diffusion tensor, and perfusion imaging in the classification of brain tumors using machine learning scheme. Neuroradiology 61, 757-765.

Smirniotopoulos, J.G., Murphy, F.M., Rushing, E.J., Rees, J.H., and Schroeder, J.W. (2007). Patterns of contrast enhancement in the brain and meninges. Radiographics 27, 525-551.

Stadlbauer, A., Merkel, A., Zimmermann, M., Sommer, B., Buchfelder, M., Meyer-Base, A., and Rossler, K. (2017a). Intraoperative Magnetic Resonance Imaging of Cerebral Oxygen Metabolism During Resection of Brain Lesions. World Neurosurg *100*, 388-394.

Stadlbauer, A., Oberndorfer, S., Zimmermann, M., Renner, B., Buchfelder, M., Heinz, G., Doerfler, A., Kleindienst, A., and Roessler, K. (2020). Physiologic MR imaging of the tumor microenvironment revealed switching of metabolic phenotype upon recurrence of glioblastoma in humans. J Cereb Blood Flow Metab *40*, 528-538.

Stadlbauer, A., Zimmermann, M., Kitzwogerer, M., Oberndorfer, S., Rossler, K., Dorfler, A., Buchfelder, M., and Heinz, G. (2017b). MR Imaging-derived Oxygen Metabolism and Neovascularization Characterization for Grading and IDH Gene Mutation Detection of Gliomas. Radiology *283*, 799-809.

Stupp, R., Mason, W.P., van den Bent, M.J., Weller, M., Fisher, B., Taphoorn, M.J., Belanger, K., Brandes, A.A., Marosi, C., Bogdahn, U., et al. (2005). Radiotherapy plus concomitant and adjuvant temozolomide for glioblastoma. N Engl J Med *352*, 987-996.

Suh, C.H., Kim, H.S., Jung, S.C., Choi, C.G., and Kim, S.J. (2018). Perfusion MRI as a diagnostic biomarker for differentiating glioma from brain metastasis: a systematic review and meta-analysis. Eur Radiol 28, 3819-3831.

Suh, J.H., Kotecha, R., Chao, S.T., Ahluwalia, M.S., Sahgal, A., and Chang, E.L. (2020). Current approaches to the management of brain metastases. Nat Rev Clin Oncol 17, 279-299.

Sunwoo, L., Yun, T.J., You, S.H., Yoo, R.E., Kang, K.M., Choi, S.H., Kim, J.H., Sohn, C.H., Park, S.W., Jung, C., et al. (2016). Differentiation of Glioblastoma from Brain Metastasis: Qualitative and Quantitative Analysis Using Arterial Spin Labeling MR Imaging. PLoS One 11, e0166662.

Swinburne, N.C., Schefflein, J., Sakai, Y., Oermann, E.K., Titano, J.J., Chen, I., Tadayon, S., Aggarwal, A., Doshi, A., and Nael, K. (2019). Machine learning for semi-automated classification of glioblastoma, brain metastasis and central nervous system lymphoma using magnetic resonance advanced imaging. Ann Transl Med 7, 232.

Tabouret, E., Chinot, O., Metellus, P., Tallet, A., Viens, P., and Goncalves, A. (2012). Recent trends in epidemiology of brain metastases: an overview. Anticancer Res 32, 4655-4662.

Tsolaki, E., Svolos, P., Kousi, E., Kapsalaki, E., Fountas, K., Theodorou, K., and Tsougos, I. (2013). Automated differentiation of glioblastomas from intracranial metastases using 3T MR spectroscopic and perfusion data. Int J Comput Assist Radiol Surg 8, 751-761.

van Gelderen, P., de Zwart, J.A., and Duyn, J.H. (2008). Pittfalls of MRI measurement of white matter perfusion based on arterial spin labeling. Magn Reson Med 59, 788-795.

Vaupel, P., Thews, O., and Hoeckel, M. (2001). Treatment resistance of solid tumors: role of hypoxia and anemia. Med Oncol 18, 243-259.

Warburg, O., Wind, F., and Negelein, E. (1927). The Metabolism of Tumors in the Body. J Gen Physiol 8, 519-530.

Wen, P.Y., and Kesari, S. (2008). Malignant gliomas in adults. N Engl J Med 359, 492-507.

Wiestler, B., Kluge, A., Lukas, M., Gempt, J., Ringel, F., Schlegel, J., Meyer, B., Zimmer, C., Forster, S., Pyka, T., et al. (2016). Multiparametric MRI-based differentiation of WHO grade II/III glioma and WHO grade IV glioblastoma. Sci Rep 6, 35142.

Woodworth, G., McGirt, M.J., Samdani, A., Garonzik, I., Olivi, A., and Weingart, J.D. (2005). Accuracy of frameless and frame-based image-guided stereotactic brain biopsy in the diagnosis of glioma: comparison of biopsy and open resection specimen. Neurol Res 27, 358-362.

Yablonskiy, D.A., and Haacke, E.M. (1994). Theory of NMR signal behavior in magnetically inhomogeneous tissues: the static dephasing regime. Magn Reson Med 32, 749-763.

Young, G.S. (2007). Advanced MRI of adult brain tumors. Neurol Clin 25, 947-973, viii.

7 APPENDIX

7.1 Tables

Table A1: Means ± standard deviations of oxygen extraction fraction (OEF), cerebral blood flow (CBF) and cerebral metabolic rate of oxygen (CMRO$_2$) in glioblastomas and metastases by patient and across tumor types and ROIs. OEF is calculated using the artificial neural network approach and carries over into CMRO$_2$ through CBF. CBF is identical for the ANN and X-means clustering method.

ANN Patient #	OEF [%]			CBF [ml/ 100g/ min]			CMRO2 [µmol/ 100g/ min]		
	CET	NET2	cNAB	CET	NET2	cNAB	CET	NET2	cNAB
Glioblastomas									
1	41.3 ± 19.0	26.0 ± 13.7	48.4 ± 21.7	97.7 ± 106.7	89.1 ± 100.4	98.1 ± 109.6	305.5 ± 410.9	163.2 ± 208.9	370.7 ± 503.2
2	39.7 ± 16.5	37.6 ± 10.1	42.3 ± 16.2	48.7 ± 50.9	76.2 ± 36.7	21.6 ± 26.3	147.3 ± 182.2	212.0 ± 119.7	68.0 ± 92.0
3	39.7 ± 21.9	48.9 ± 14.1	42.2 ± 19.2	40.8 ± 37.5	28.4 ± 20.8	31.2 ± 26.6	116.7 ± 130.2	99.0 ± 82.7	96.9 ± 102.8
4	32.8 ± 17.2	24.3 ± 14.1	36.3 ± 18.8	27.7 ± 25.3	11.1 ± 13.9	22.2 ± 24.0	69.9 ± 79.0	20.8 ± 33.1	60.1 ± 79.8
5	38.0 ± 15.2	27.1 ± 8.3	41.9 ± 9.8	33.6 ± 28.5	11.8 ± 12.4	28.5 ± 27.8	97.4 ± 111.5	23.6 ± 26.4	87.5 ± 91.1
6	27.5 ± 21.1	26.1 ± 14.3	39.6 ± 15.0	47.8 ± 36.7	13.0 ± 12.8	41.0 ± 35.0	107.9 ± 131.7	25.8 ± 32.2	120.2 ± 126.9
7	34.6 ± 20.6	21.8 ± 11.4	48.6 ± 10.7	59.1 ± 42.7	26.0 ± 19.2	33.7 ± 31.0	153.2 ± 175.5	43.2 ± 46.9	118.7 ± 114.6
mean	36.2 ± 4.9	30.3 ± 9.6	42.8 ± 4.4	50.8 ± 23.1	36.5 ± 32.5	39.5 ± 26.7	142.5 ± 77.3	84.0 ± 77.0	131.7 ± 107.8
Metastases									
1	43.3 ± 13.6	26.0 ± 12.2	48.4 ± 12.9	51.2 ± 57.0	18.3 ± 20.9	37.2 ± 50.0	162.3 ± 199.3	35.9 ± 50.1	137.2 ± 194.0
2	43.0 ± 18.5	20.4 ± 15.1	47.4 ± 16.4	55.0 ± 23.5	8.5 ± 12.0	42.6 ± 18.1	171.9 ± 110.3	13.8 ± 30.7	148.5 ± 85.7
3	32.3 ± 17.6	31.5 ± 15.5	43.3 ± 16.6	63.4 ± 41.4	12.7 ± 13.2	46.8 ± 38.6	155.3 ± 138.9	29.9 ± 39.3	143.5 ± 138.8
4	45.8 ± 10.1	39.1 ± 7.5	62.5 ± 10.7	53.7 ± 47.8	14.3 ± 14.9	14.1 ± 21.1	173.4 ± 161.1	41.3 ± 42.5	63.3 ± 96.0
5	55.4 ± 27.1	19.6 ± 13.5	41.9 ± 5.3	98.5 ± 88.6	40.7 ± 38.1	38.7 ± 35.3	425.9 ± 498.1	60.2 ± 100.7	122.1 ± 118.9
6	38.2 ± 15.3	33.6 ± 12.0	56.9 ± 15.4	48.3 ± 53.1	5.9 ± 16.9	24.9 ± 35.3	131.0 ± 158.9	16.2 ± 49.9	102.0 ± 150.1
7	43.2 ± 21.8	26.2 ± 17.9	38.2 ± 17.5	52.4 ± 55.6	9.4 ± 13.0	35.6 ± 34.8	173.5 ± 231.2	20.0 ± 33.6	100.1 ± 124.7
8	49.8 ± 20.0	30.4 ± 9.1	44.2 ± 14.8	16.7 ± 27.6	13.3 ± 17.1	14.9 ± 19.9	67.3 ± 154.0	28.6 ± 39.3	49.9 ± 74.5
mean	43.9 ± 7.0	28.3 ± 6.6	47.9 ± 8.1	54.9 ± 22.4	15.4 ± 10.9	31.8 ± 12.4	182.6 ± 104.6	30.7 ± 15.2	108.3 ± 36.7

Table A2: Means ± standard deviations of oxygen extraction fraction (OEF), cerebral blood flow (CBF) and cerebral metabolic rate of oxygen ($CMRO_2$) in glioblastomas and metastases by patient and across tumor types and ROIs. OEF is calculated using the X-means clustering approach and carries over into $CMRO_2$ through CBF. CBF is identical for the ANN and X-means clustering method.

| Cluster	OEF [%]			CBF [ml/100g/min]			$CMRO_2$ [µmol/100g/min]		
Patient #	CET	NET2	cNAB	CET	NET2	cNAB	CET	NET2	cNAB
Glioblastomas									
1	26.6 ± 9.6	24.0 ± 9.0	27.2 ± 9.2	97.7 ± 106.7	89.1 ± 100.4	98.1 ± 109.6	263.5 ± 369.3	222.9 ± 350.2	265.8 ± 410.3
2	37.8 ± 11.2	45.3 ± 8.6	34.6 ± 8.0	48.7 ± 50.9	76.2 ± 36.7	21.6 ± 26.3	169.9 ± 227.9	275.1 ± 177.9	65.9 ± 93.1
3	27.9 ± 9.6	31.3 ± 5.4	29.8 ± 7.6	40.8 ± 37.5	28.4 ± 20.8	31.2 ± 26.6	96.2 ± 108.9	71.1 ± 59.8	77.2 ± 76.7
4	31.7 ± 9.7	24.8 ± 7.0	32.9 ± 9.7	27.7 ± 25.3	11.1 ± 13.9	22.2 ± 24.0	76.6 ± 83.6	25.5 ± 38.5	63.6 ± 80.7
5	32.5 ± 7.8	23.6 ± 4.6	35.3 ± 8.1	33.6 ± 28.5	11.8 ± 12.4	28.5 ± 27.8	91.8 ± 92.1	23.4 ± 27.3	89.6 ± 99.4
6	26.4 ± 11.7	19.5 ± 5.4	31.4 ± 7.4	47.8 ± 36.7	13.0 ± 12.8	41.0 ± 35.0	115.4 ± 128.3	21.5 ± 24.7	106.3 ± 112.0
7	21.2 ± 8.5	12.8 ± 4.9	23.9 ± 5.5	59.1 ± 42.7	26.0 ± 19.2	33.7 ± 31.0	103.7 ± 118.0	28.1 ± 30.8	69.0 ± 74.6
mean	29.2 ± 5.3	25.9 ± 10.2	30.7 ± 4.1	50.8 ± 23.1	36.5 ± 32.5	39.5 ± 26.7	131.0 ± 65.5	95.4 ± 107.4	105.3 ± 72.3
Metastases									
1	38.9 ± 4.6	30.3 ± 3.2	40.3 ± 4.0	51.2 ± 57.0	18.3 ± 20.9	37.2 ± 50.0	145.7 ± 158.7	41.6 ± 48.9	110.4 ± 148.9
2	32.4 ± 6.5	15.6 ± 4.6	30.8 ± 5.4	55.0 ± 23.5	8.5 ± 12.0	42.6 ± 18.1	139.9 ± 76.6	13.0 ± 23.4	102.0 ± 54.5
3	34.3 ± 9.7	21.7 ± 7.0	36.4 ± 8.8	63.4 ± 41.4	12.7 ± 13.2	46.8 ± 38.6	177.9 ± 137.2	24.1 ± 30.5	142.5 ± 137.0
4	36.0 ± 2.2	35.1 ± 1.8	36.8 ± 2.5	53.7 ± 47.8	14.3 ± 14.9	14.1 ± 21.1	146.2 ± 133.2	37.4 ± 39.2	38.8 ± 58.9
5	40.1 ± 13.2	24.1 ± 9.1	32.1 ± 9.0	98.5 ± 88.6	40.7 ± 38.1	38.7 ± 35.3	348.7 ± 391.1	92.1 ± 132.8	113.9 ± 124.2
6	34.0 ± 10.0	23.6 ± 7.6	36.4 ± 7.2	48.3 ± 53.1	5.9 ± 16.9	24.9 ± 35.3	146.1 ± 186.3	15.6 ± 52.0	81.7 ± 129.0
7	25.6 ± 9.3	15.8 ± 5.9	23.1 ± 7.3	52.4 ± 55.6	9.4 ± 13.0	35.6 ± 34.8	121.1 ± 172.2	13.5 ± 21.2	70.0 ± 82.7
8	23.3 ± 4.5	16.2 ± 3.8	22.2 ± 5.0	16.7 ± 27.6	13.3 ± 17.1	14.9 ± 19.9	29.8 ± 51.0	17.7 ± 25.1	27.1 ± 40.7
mean	33.1 ± 5.9	22.8 ± 7.1	32.3 ± 6.6	54.9 ± 22.4	15.4 ± 10.9	31.8 ± 12.4	156.9 ± 88.9	31.9 ± 26.7	85.8 ± 39.3

7.2 ROC curves
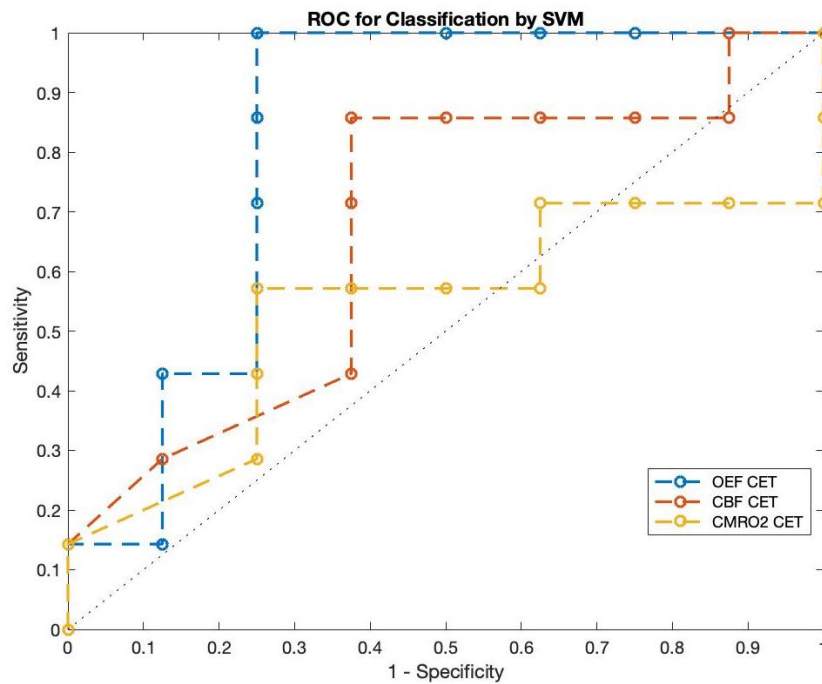
Figure A1: Five-fold cross-validated receiver operating characteristic (ROC) curves for the linear kernel support-vector machine classifier predicting binary outcome (glioblastoma or metastasis). Curves are shown for oxygen extraction fraction (OEF, blue), cerebral blood flow (CBF, orange) and cerebral metabolic rate of oxygen (CMRO$_2$, yellow) in contrast-enhancing tumor (CET).
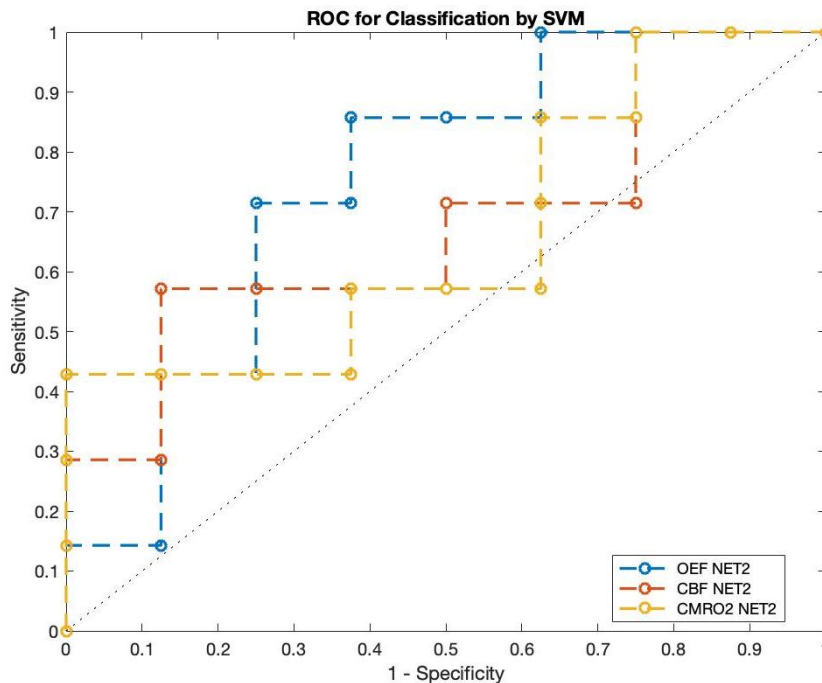

Figure A2: Five-fold cross-validated receiver operating characteristic (ROC) curves for the linear kernel support-vector machine classifier predicting binary outcome (glioblastoma or metastasis). Curves are shown for oxygen extraction fraction (OEF, blue), cerebral blood flow (CBF, orange) and cerebral metabolic rate of oxygen (CMRO$_2$, yellow) in the peritumoral non-enhancing T2 FLAIR hyperintense (NET2) region of interest.

APPENDIX
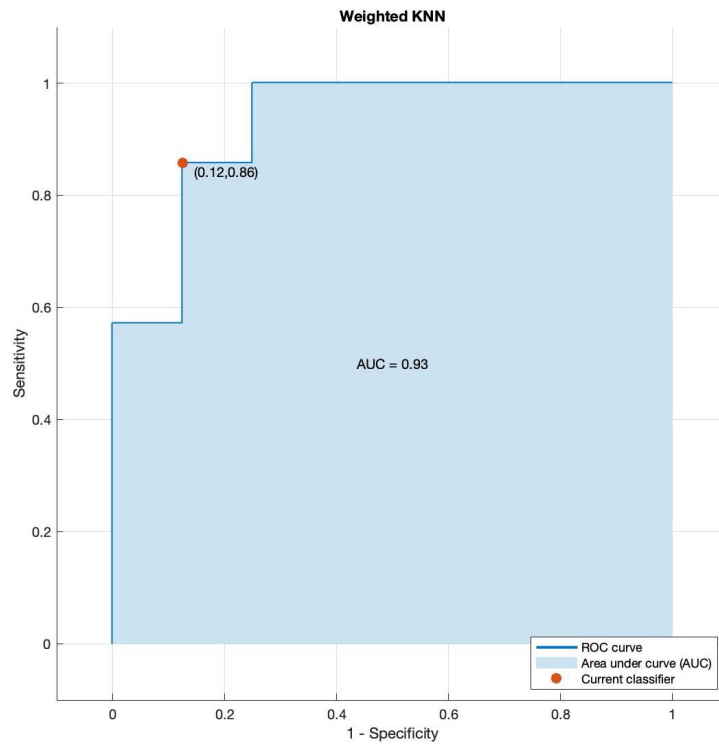
Figure A3: Five-fold cross-validated receiver operating characteristic (ROC) curve for the weighted k-nearest neighbour (KNN) classifier predicting binary outcome (glioblastoma or metastasis). The curve shows the classification performance of a multivariable prediction using the two features OEF_{CET} and $CMRO_{2\ CET/NET2}$. Area under the curve is 0.93, accuracy is 87%, optimal sensitivity and specificity are 86% and 88%, respectively.
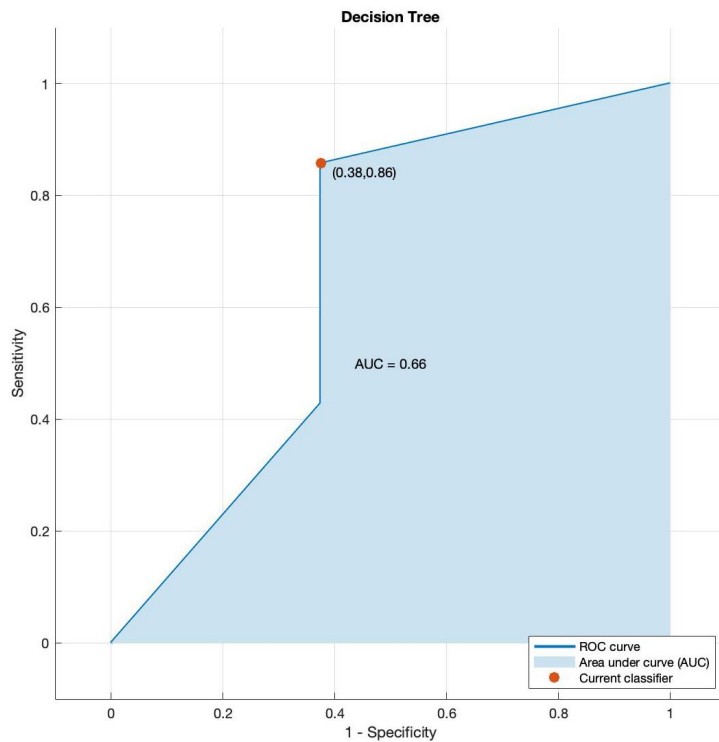
Figure A4: Five-fold cross-validated receiver operating characteristic (ROC) curve for the decision tree classifier predicting binary outcome (glioblastoma or metastasis). The curve shows the classification performance of a multivariable prediction using the two features OEF_{CET} and $CMRO_{2\ CET/NET2}$. Area under the curve is 0.66, accuracy is 73%, optimal sensitivity and specificity are 86% and 62%, respectively.
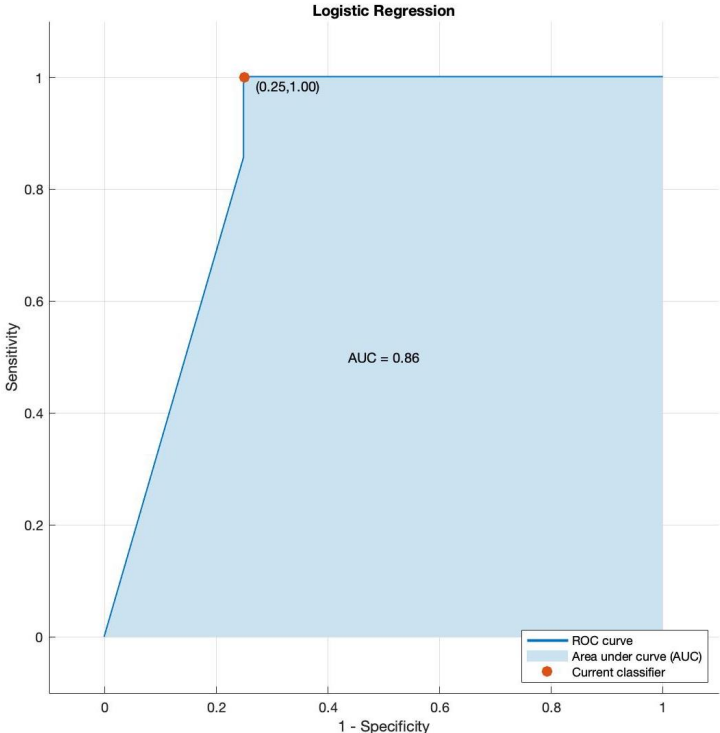
Figure A5: Five-fold cross-validated receiver operating characteristic (ROC) curve for the logistic re-gression classifier predicting binary outcome (glioblastoma or metastasis). The curve shows the classification performance of a multivariable prediction using the two features OEF_{CET} and $CMRO_{2\ CET/NET2}$. Area under the curve is 0.86, accuracy is 87%, optimal sensitivity and specificity are 100% and 75%, respectively.
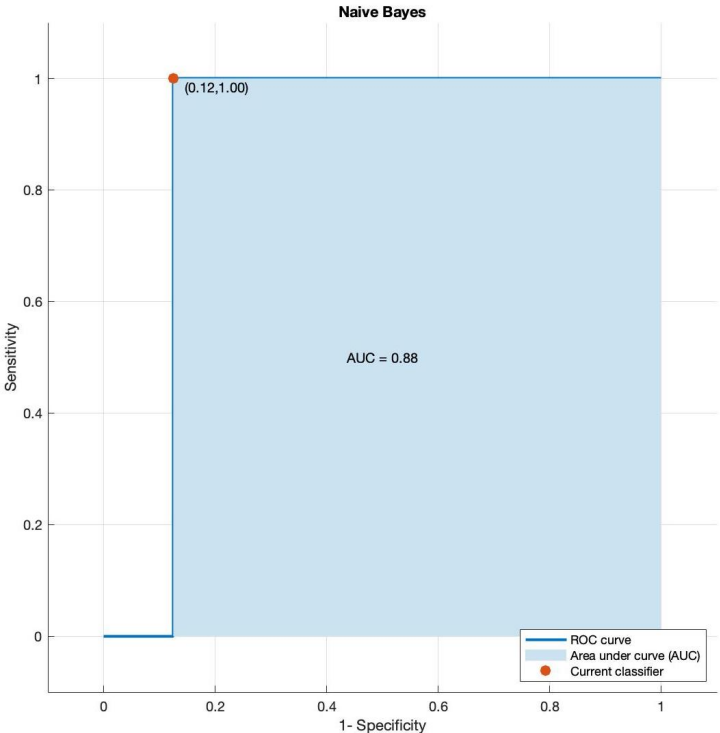
Figure A6: Five-fold cross-validated receiver operating characteristic (ROC) curve for the Naïve Bayes classifier predicting binary outcome (glioblastoma or metastasis). The curve shows the clas-sification performance of a multivariable prediction using the two features OEF_{CET} and $CMRO_{2\ CET/NET2}$. Area under the curve is 0.88, accuracy is 93%, optimal sensitivity and spec-ificity are 100% and 88%, respectively.
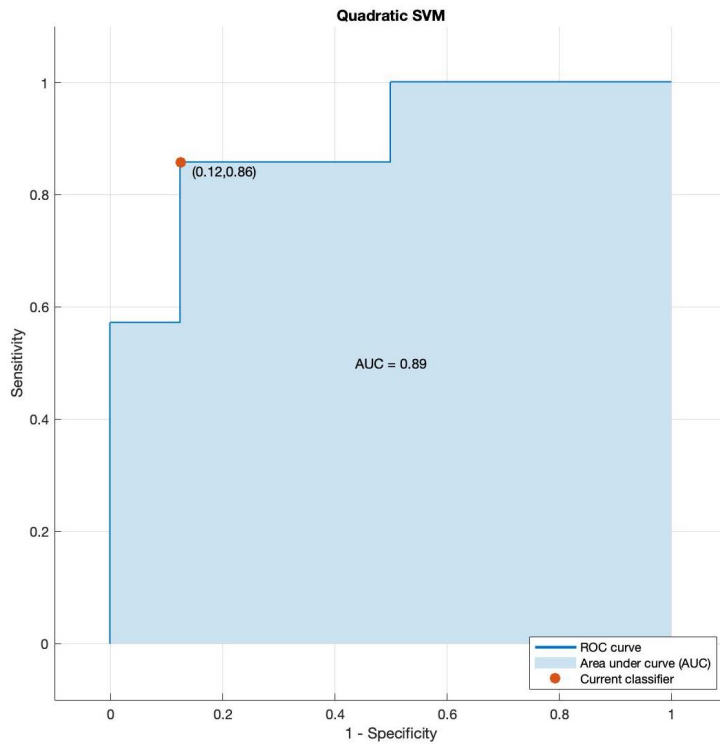
Figure A7: Five-fold cross-validated receiver operating characteristic (ROC) curve for the quadratic kernel support-vector machine (SVM) classifier predicting binary outcome (glioblastoma or metastasis). The curve shows the classification performance of a multivariable prediction using the two features OEF_{CET} and $CMRO_{2\ CET/NET2}$. Area under the curve is 0.89, accuracy is 87%, optimal sensitivity and specificity are 86% and 88%, respectively.
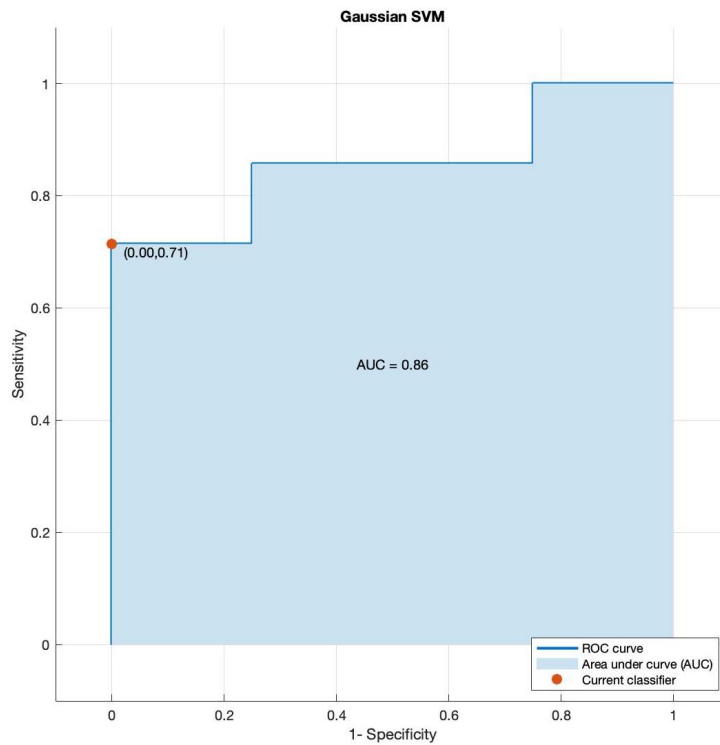
Figure A8: Five-fold cross-validated receiver operating characteristic (ROC) curve for the Gaussian kernel support-vector machine (SVM) classifier predicting binary outcome (glioblastoma or metastasis). The curve shows the classification performance of a multivariable prediction using the two features OEF_{CET} and $CMRO_{2\ CET/NET2}$. Area under the curve is 0.86, accuracy is 87%, optimal sensitivity and specificity are 71% and 100%, respectively.

8   CURRICULUM VITAE

PERSONAL DETAILS

Name:	Baazaoui, Hakim
Date of birth:	27.04.1994
Place of birth:	Bad Soden am Taunus
Father:	Moncef Baazaoui
Mother:	Ulrike Johanna Berges-Baazaoui

FORMAL EDUCATION

2004 – 2012	High school: Kaiserin-Friedrich-Gymnasium, Bad Homburg vor der Höhe
Jun 2012	High school diploma (Abitur, GPA: 1.3)

HIGHER EDUCATION

WS 2012/13	Start of undergraduate studies: Bachelor of Arts in Economics at the University of St. Gallen (Switzerland)
	Bachelor thesis: *Epidemiological Considerations on the Current Outbreak of Ebolavirus Disease in the Republic of Guinea*
Mar 2016	Bachelor of Arts – Economics (GPA: 5.13/6)
WS 2016/17	Start of medical studies at the Medical Faculty Mannheim, Heidelberg University
Sep 2018	Passed first state examination (grade: very good)
Oct 2021	Passed second state examination (grade: good)

9 ACKNOWLEDGEMENTS